Chapter 4 Experimental Setup and equipment

4.1 Introduction

For the current research, construction of a wind tunnel airfoil model with a leading/trailing edge flap actuator was performed. The model is instrumented in order to measure pressure, and forces. Both are used to show the overall improvement of the actuation system on the airfoil performance. The related description of the equipment used in this experiment is provided in the following sections. A valuable source of information regarding construction, instrumentation and set up for wind tunnel testing is Barlow *et al.* (1999).

4.2 Wind Tunnel

The Engineering Science and Mechanics Wind Tunnel is an open-circuit low-speed tunnel, constructed in 1983. A schematic drawing is shown in Figure 4.2.1.

For inlet flow turbulence control one honeycomb and five nylon flow conditioning screens are included in the settling chamber. A 5 to 1 contraction ratio follows the settling chamber. The test section is 0.51m by 0.51m and 1.27m in length, having a working area with an easily removable Plexiglas wall in the side for convenient tunnel access and visualization. The top wall is also made of Plexiglas to accommodate light sources for use in flow visualization. The wind tunnel diffuser is angled at 5° and carries an area ratio of 3.7.

A pitot tube is mounted on the far wall and connected to the Edwards-Datametrics Barocell precision pressure transducer, giving the freestream dynamic pressure reading (i.e.: velocity) on the test section. The Barocell model 590D-100T-3Q8-H5X-4D was used in conjunction with a model 1450 Electronic Manometer, providing a LED readout of the pressure. The Barocell has a range of 100 Torr and a resolution of 0.01% of full scale. The stated accuracy of the Barocell is 0.05% of the reading plus 0.001% of the full scale. Freestream velocities can range from 4 m/sec to 20 m/sec via an axial fan driven by a 5 hp dc motor. Both the fan and motor are mounted on a concrete isolation block to reduce the transfer of vibration to the tunnel walls. The generated velocities are very stable over time and the maximum turbulence intensity is 1.25%. The flow across the test section is reasonably uniform with a variation smaller than 2.5%. More details regarding the design, construction and calibration of this facility can be found in the report by Seider (1984).

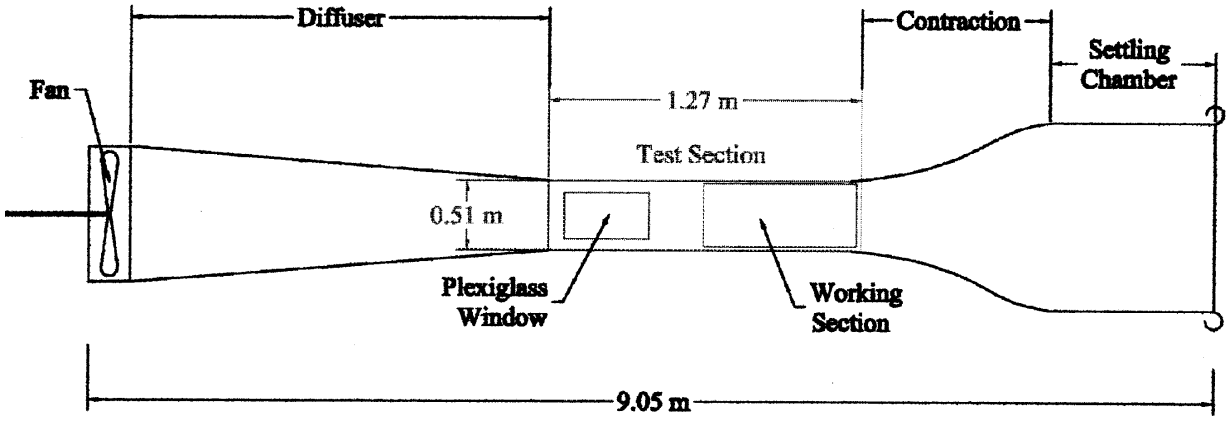

Figure 4.2.1 ESM Wind Tunnel. From Seider (1984)

Some necessary modifications where performed on the tunnel walls for the installation of the airfoil and rake. A 30 cm by 3 cm slot was perforated along the centerline of the bottom wall at the end of the test section, to accommodate the pitot rake. A traversing mechanism was positioned beneath the wall and to a side of the slot to attach the rake and traverse it to the required position. This will become eventually more clear as the pitot rake is discussed. A slot was also machined on the Plexiglas side on the test section, to extend the airfoil shaft to the support outside the tunnel.

A rotary table was constructed on the plywood far wall. There are two reasons for this:

a) The airfoil pressure transducer has to be as close to the pressure taps as possible to increase the frequency response. Space inside the airfoil restricted the installation to a location outside the model. At the same time, installation on the airfoil shaft was to be avoided to reduce the model's natural frequency affecting the balance readings. The only alternative was to mount the transducer on the wall. Since the angle of attack is variable and a physical connection exist to the closely fitted pressure taps tubing, a rotary table is a must to avoid pressure tubes warping or stretching.

b) The flap actuation mechanism extends outside the tunnel near the leading or trailing edge of the airfoil. Since the angle of attack is varied, a rotary table is needed to accommodate the airfoil to a new position.

The rotary table is two centimeters larger in diameter than the airfoil chord.

4.3 Airfoil model and instrumentation

4.3.1 Airfoil Model

The model section is a symmetrical circular-arc 8 percent chord thickness airfoil. The chord length is 0.2032 m (8 in) resulting in an airfoil maximum thickness of 0.0162 m (0.64 in). The model spans 0.5080 m (20 in), 2 mm less than the tunnel width. The airfoil contour geometry is defined by a circular-arc of radius 63.9 cm (25.16 in).

The model was constructed by traditional composite-structure manufacturing techniques in order to create a strong thin walled structure to accommodate the pressure taps in such a slim airfoil. Fiberglass fiber and polyester resin were positioned on a female mold of half the thickness of the wing. Two parts were produced completing the airfoil model. The flap, flap driving rod, and airfoil edges plate parts were copied on the female mold in order to create the required spaces on the fabricated parts, reducing *a posteriori* work. This will become more clear as the flap system is described later.

A 9.525 mm (3/8”) diameter aircraft grade aluminum hollow rod serves as a structural spar on the model, and it’s positioned in the 50 percent chord of the airfoil. The structural member extends on both sides of the airfoil to link the model to the support points. Model geometry and dimensions are shown in Figures 4.3.1.1 and 4.3.1.2.

A total of 61 pressure taps where installed on the airfoil, 30 on the suction side and 31 on the pressure side. These were constructed from 0.7112 mm (0.028“) outer diameter and 0.4064 mm (0.016“) inner diameter stainless steel tubing, having an approximate length of 60 mm. The steel tubes were carefully bent in their tip to be able to tightly fit in the airfoil interior. Holes were drilled and the tubes epoxied to the airfoil skin. The pressure taps are positioned with an offset angle of 5° with respect to the perpendicular of the spanwise axis of the airfoil model, as shown in Figure 4.3.1.1 . This is done to avoid any aerodynamic interference between pressure taps, even when they were carefully installed in the airfoil contour surface. The suction side surface pressure taps are rotated clockwise and the pressure side ones counterclockwise. This asymmetry was needed to make room inside the model for the tubing connections. Tygon R-3603 tubing of 2.38 mm (3/32”) outer diameter and 0.79 mm (1/32”) inner diameter are connected to each stainless steel tap end and directed outside the tunnel through one of airfoil’s ends.

Figure 4.3.1.3 shows the opened airfoil model halves to clarify the described construction. The flap actuating/sensing mechanism is shown on the top-right side of the picture and will be described later.

A Pressure Systems Incorporated ESP Pressure Scanner is attached to the rotary wall of the Wind tunnel and used to measure the pressures over the airfoil. The Tygon tubing length is kept as short as possible in order to minimize frequency response reduction due to tubing damping. The ideal is to place the pressure sensor inside the wing, but due to the physical limitations, this was impossible.

The ESP pressure scanner utilized in the current research is a 32 Channel model with ±10 inches of water column pressure range. When properly calibrated, the ESP has an accuracy of 0.10% of the full scale and an acceleration response of ±0.008% of full scale per G. A photograph of an 32 channel ESP can be seen in Figure 4.3.1.4.

Since holes and slots were fabricated, air tends to be drawn into the tunnel from the test section. Apart of closing all possible openings after the set up was installed, air entrainment from the slots for the airfoil shaft on the sides of the tunnel couldn't be avoided. Tampering with the balance proper function would occur if the airfoil model were linked somehow to the tunnel walls.

To remedy this, endplates were fabricated at the airfoil model, to avoid flow perturbation from airflow entrainment coming from outside the tunnel. This were also necessary for creating a better two dimensional flow, eliminating wingtip vortices and helping to reduce the tunnel boundary layer detrimental effects.

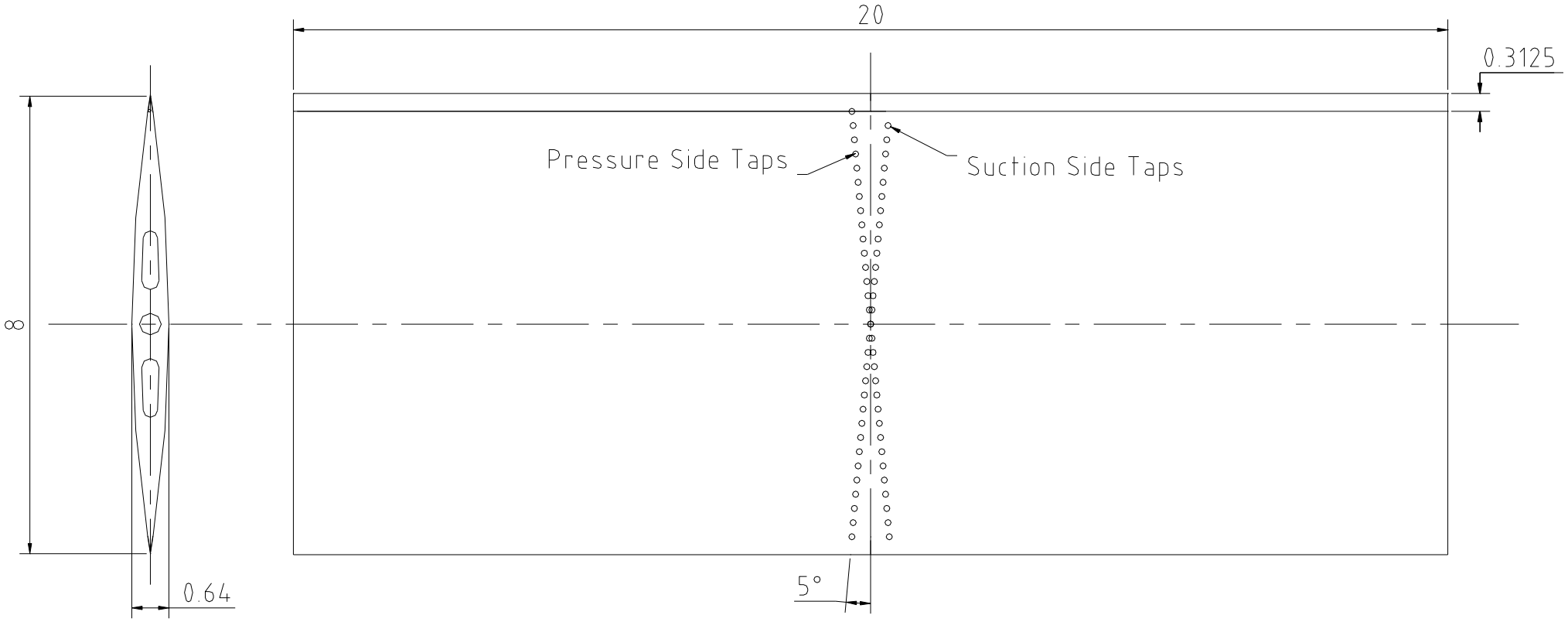

Figure 4.3.1.1 Airfoil model dimensions (in inches)

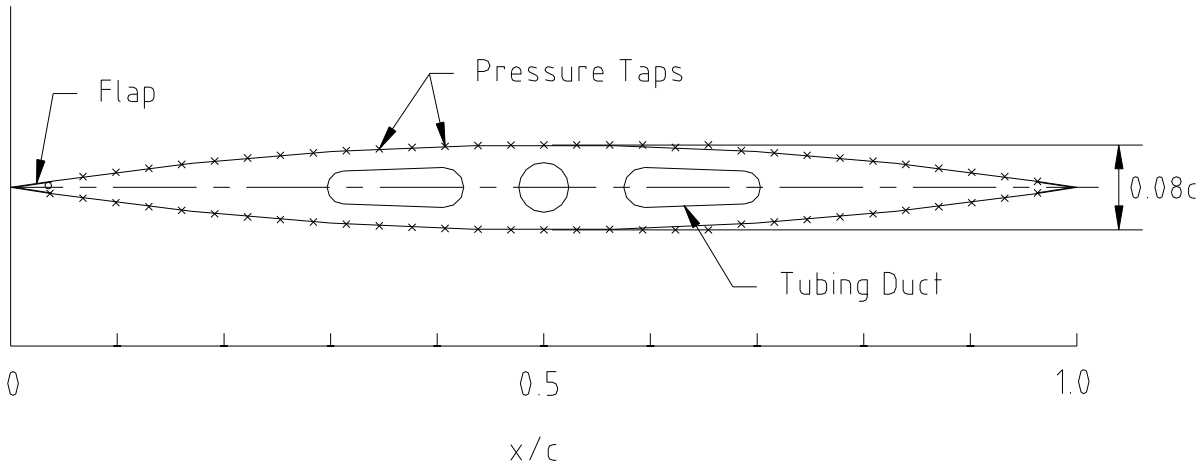

Figure 4.3.1.2 Model geometry and pressure taps location

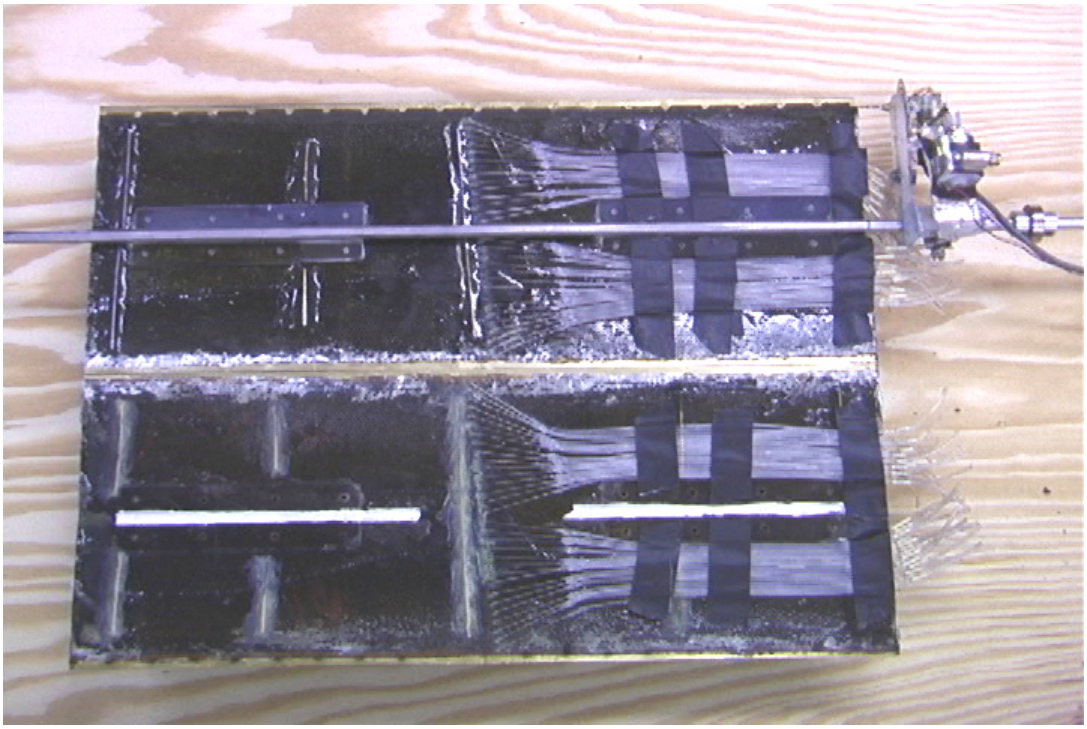

Figure 4.3.1.3 Pressure taps construction

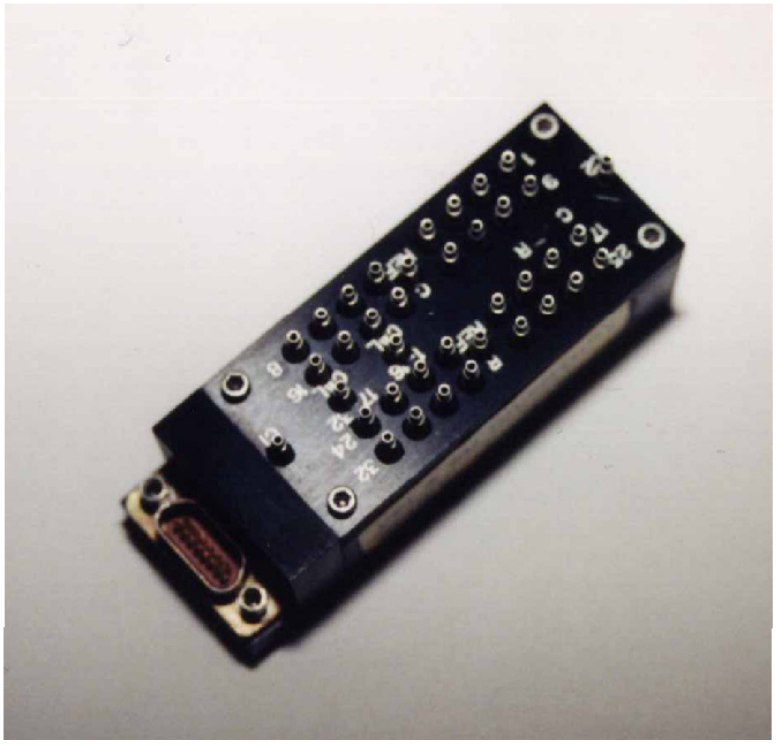

Figure 4.3.1.4 32 Channel PSI ESP Pressure Scanner

4.3.2 Actuation System

The actuation system consists of a flat plate of 4 percent airfoil chord length extending the whole model span. The thickness of the plate is 0.127 mm (0.0050 in) and is made out of brass. The flat plate is attached at one of its ends to a 1.27 mm (0.05 in) diameter stainless steel rod, that works as the structural connection between the flap and the wing and at the same time allows the rotational movement of the flap. The rod is longer than the model span in order to link from one side of the tunnel the actuating mechanism.
Slots in the flap and close to the rod were fabricated in order to create the hinges to support the flap to the wing. Figure 4.3.2.1 shows a picture of the actual model flap and slots, with the connection hinges.

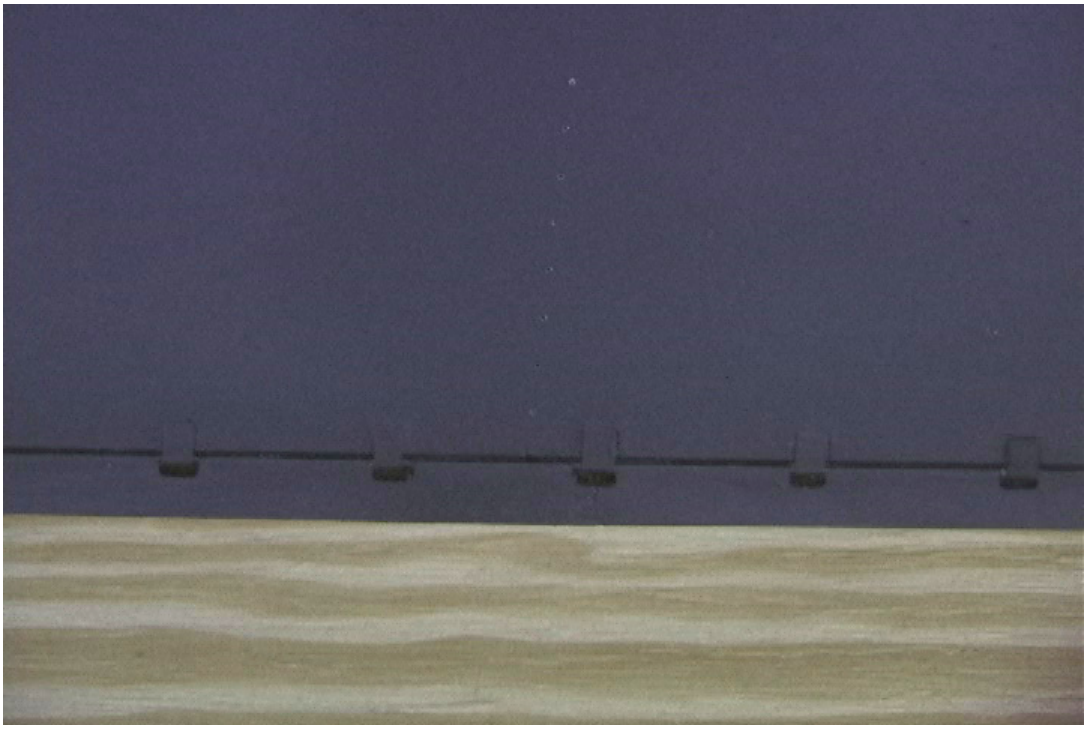

Figure 4.3.2.1 Flap close up view

The flap as shown is placed on one of the edges of the airfoil model. In its closed position, the flap edge forms one of the sides of the airfoil edges (i.e.: it doesn't extend over the airfoil edge). Since the airfoil model is symmetric, the flap can be placed on any side and edge for testing without having to change parts or disassembling the model. In this work, the flap was always placed on the suction side of the airfoil, and the chord position was changed between the leading edge and the trailing edge.

The flap rotation goes from the fully closed position, where the original clean airfoil shape is obtained, to a maximum amplitude q of around 60 degrees. The schematic of this is shown in Figure 4.3.2.2.

The flap is oscillated in a sinusoidal motion by a DC motor and an eccentric arrangement. This is shown schematically in Figure 4.3.3.1. The motor shaft is connected to a flywheel having an eccentric shaft onto it. This is the heart of the motion mechanism. A connecting rod was attached to the eccentric mechanism and operated an adjustable length bell crank fixed to the flap rod. This adjustable property gave the possibility of changing the flap amplitude. For the current research, the amplitude was fixed at 17 ±1 °.

The flywheel was balanced statically to work with minimum vibrations at speeds in the order of 100 Hertz.

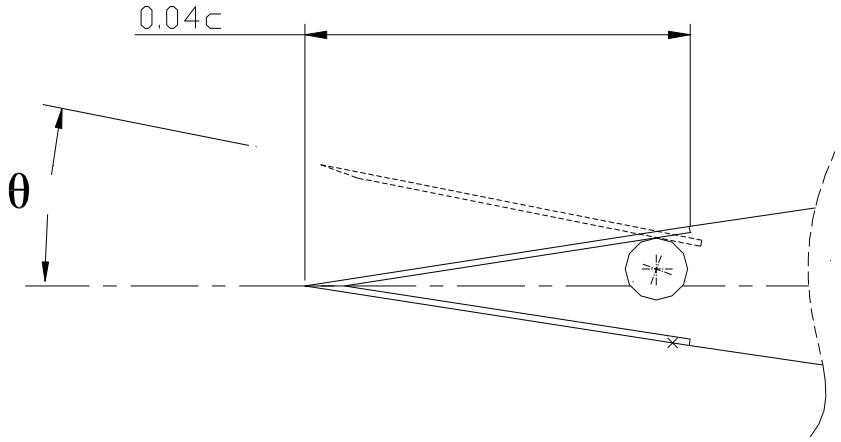

Figure 4.3.2.2 Flap Detail

The electric motor is a Radio Shack High-Speed 12 VDC Motor. At maximum efficiency the motor is capable of 11,500 rpm at 1.3 Amps and delivering a torque of 56 gm·cm. A speed controller was custom built in order to accurately change the speed from ~10 Hz to ~120 Hz (maximum tested). The controller circuit is given in Figure 4.3.2.3.

4.3.3 Feedback Sensor

Since the adjustment of the flap oscillation is performed manually, a feedback sensor is needed to permit the correct rpm motor setting. For this reason, an optical sensing system was built to be able to accomplish this. A position sensor detector (PSD) is used in conjunction with a laser pointer to give the exact position of the flap with respect to time.

The position sensing detectors are silicon photodiodes that provide an output directly proportional to the position of a light spot on the detector active area. For this research, the On-Trak Photonics 2L10-2 Duo-Lateral two-dimensional PSD is utilized. Only one dimension is used.

The laser system is based on a Radio Shack Underline Laser Pointer, delivering <5 mW of output at a wavelength of 630-670 nm. The device was completely disassembled

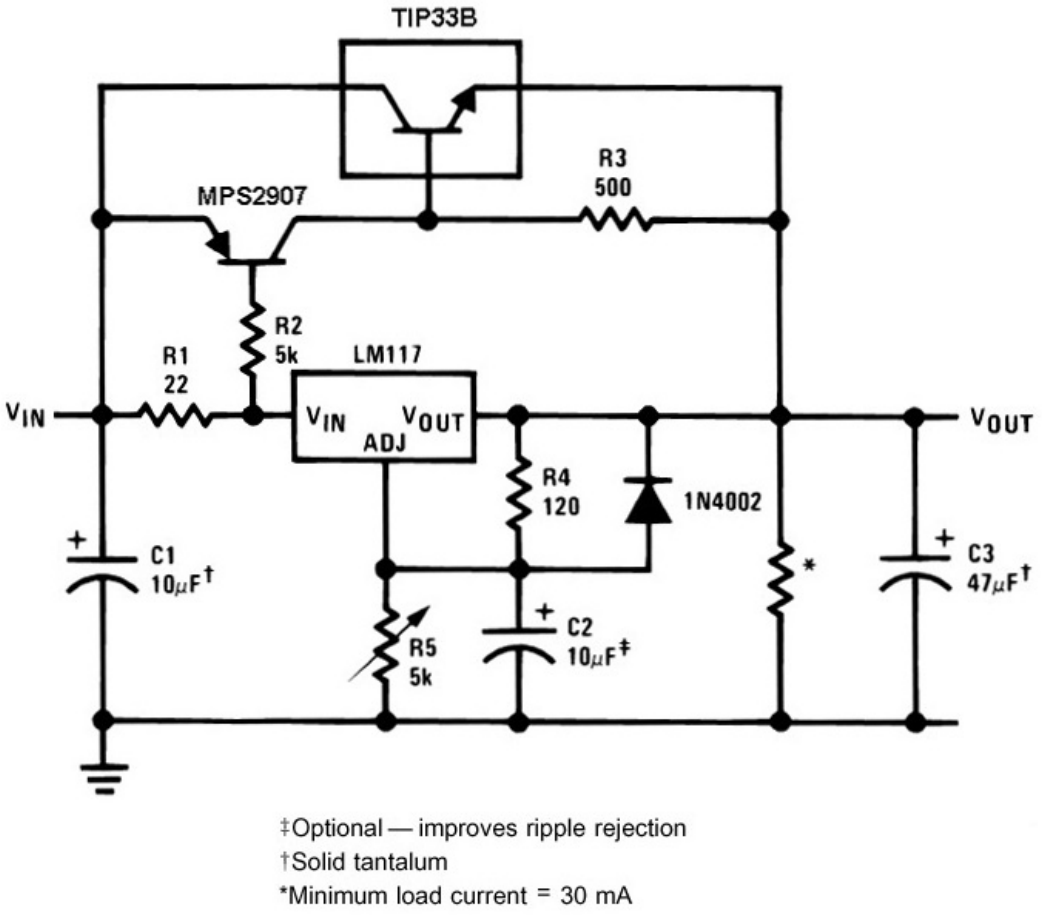

Figure 4.3.2.3 High current adjustable voltage regulator

and the batteries and external body were removed from the laser diodes and optics. In this way, a lightweight light source can be attached to the airfoil model. This is desired since the total mass of the model needs to be kept small to tailor the natural frequency of vibration. The laser diodes and optics were placed in a small plastic tube and attached close to the PSD and mirror setup. Wires were connected between the laser terminals and the batteries and a switch was also included.

The laser beam emanating from the laser pointer impinges on a small mirror attached on the flap-driving rod. The reflected beam hits the PSD, which is positioned at a distance, allowing the entire sensor photoelectric array to be used. In this way, knowing the set up geometry, a precise flap location can be given at any time. This is shown in Figure 4.3.3.1.

A picture of the complete model is shown in Figure 4.3.3.2, showing endplates and actuating/sensing mechanism on the right side of the model. A close up view of the actuating/sensing mechanism is shown in Figure 4.3.3.3.

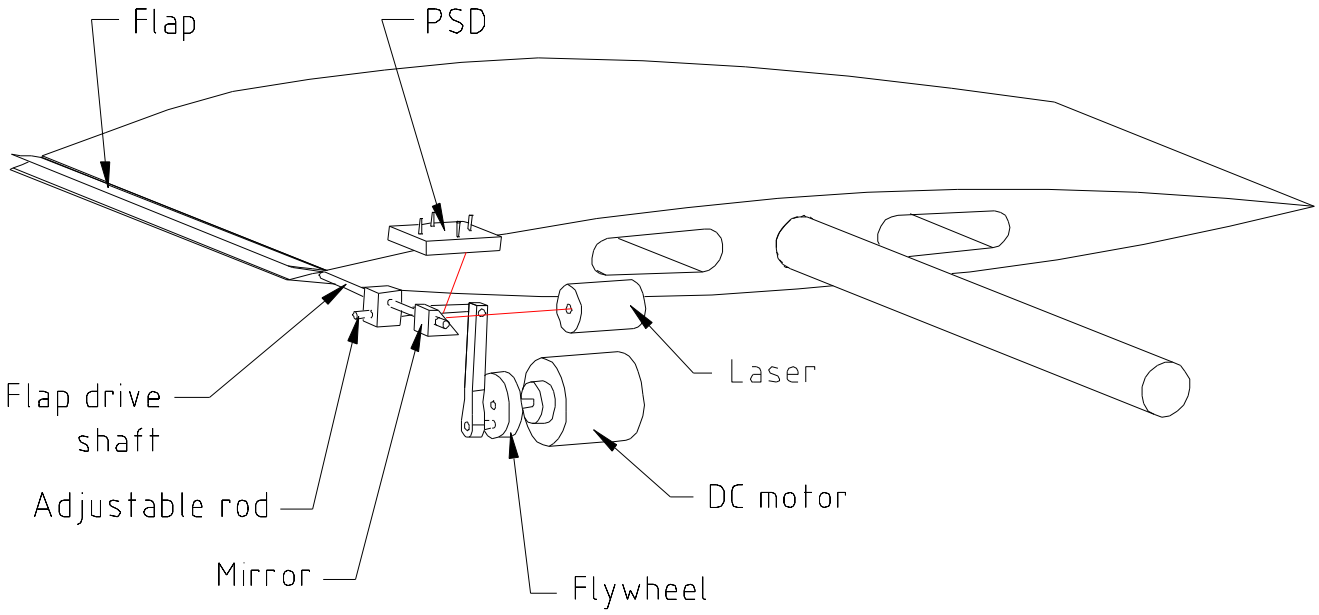

Figure 4.3.3.1 Complete model schematic

4.3.4 Strain Gage Balance

As already mentioned before, this experiment involves two forms of measuring the aerodynamic response to the flap actuation, pressure and force readings. For the latter, a strain gage balance was designed and constructed especially to be utilized on the experiment. The measuring system is based on the work done by Vlachos *et al* (1999).

The idea of having a simple but at the same time robust system for measuring forces on a wind tunnel is always appealing, and this was the goal when the project was started. The device is a multi-component balance capable of sensing six degrees of freedom on a model, by measuring strains on a load cell attached to the model. The strains are converted to voltage signals by means of strain gages mounted on the load cell.

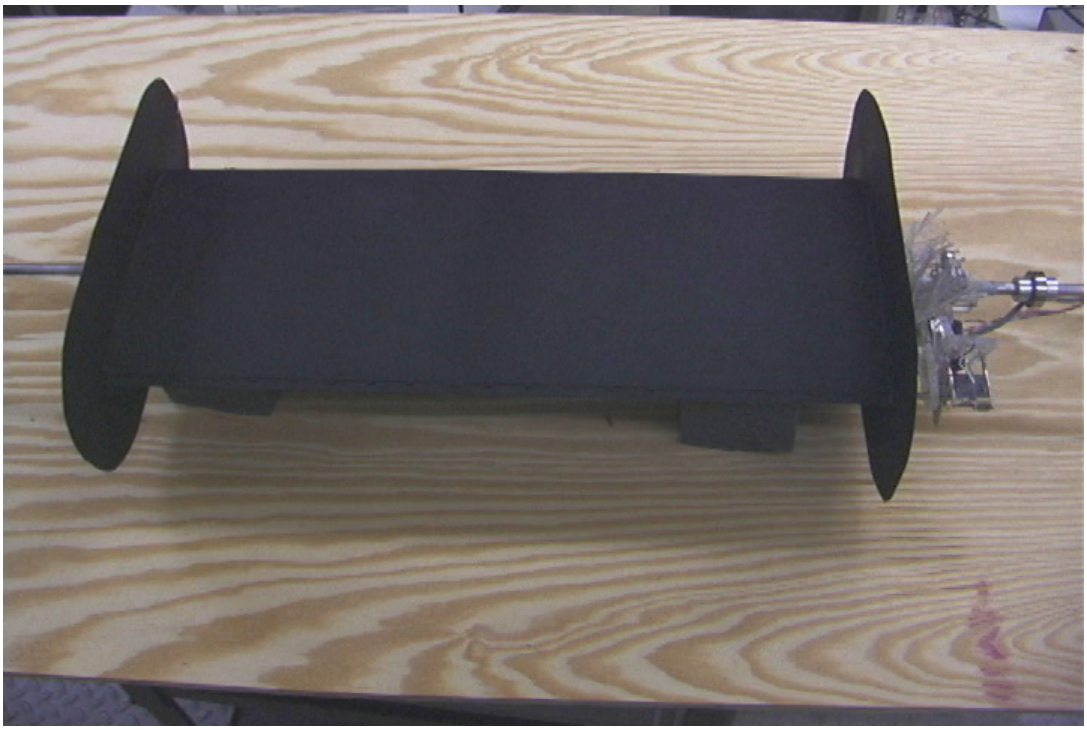

Figure 4.3.3.2 Complete airfoil model

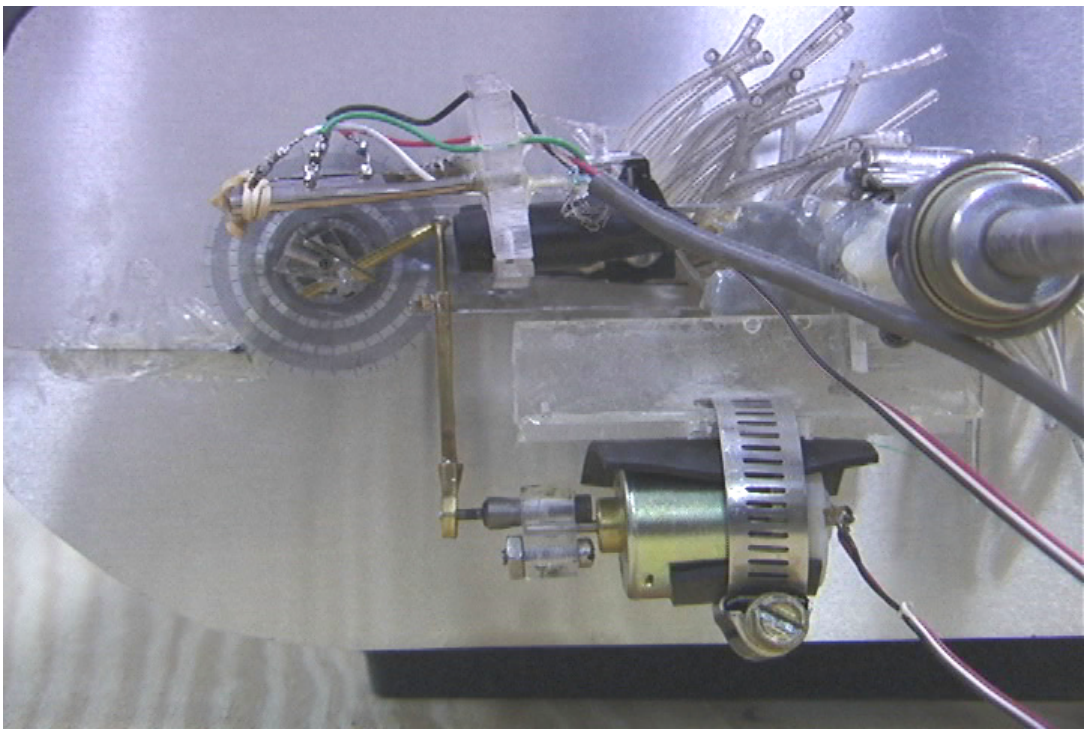

Figure 4.3.3.3 Close up view of the actuating/sensing mechanism

For this experiment a square 20 by 20 mm section hollow load cell was utilized, machined from a 7075-T6 aluminum alloy billet. Strain gages where positioned on the faces of the cell as shown on Figure 4.3.4.1. For the sake of drawing clarity, the hidden sides are not shown. It should be mentioned though, that the strain gages positioned on those sides, mirror the opposite face. In this way, strain sensor *pairs* are formed in the parallel faces. With this set up, normal and tangential forces exerted on the load cell will lead for the face-opposite strain gages to have equal magnitude of strains but different signs. This was done with the purpose to create a full bridge connection. Earlier efforts to construct load cells were not successful, because of the lack of strain sensitivity required for this experiment. This new connection increases in a 400 percent the signal output from any given load compared to the quarter bridge connection previously utilized.

Each strain gage shown in the figure, is a Dual Pattern 350±0.2 Ohms Micro-Measurements gage. This implies that each strain gage has two parallel grids, acting independently and working as two gages in one. Therefore, the number of sensing elements in the load cell totals 24. By using each strain gage *pair* to create a full bridge connection, gives the balance 6 channels capable of measuring torque and normal forces.

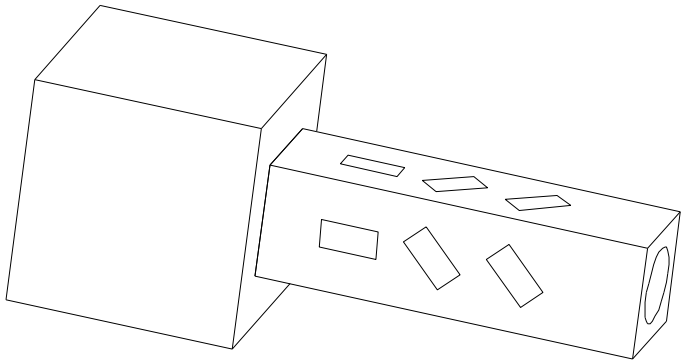

Figure 4.3.4.1 Strain Gage Balance

As the drawing shows, four strain gages were positioned normal to the longitudinal axis of the balance to capture normal strains exerted on the cell surface. The rest of the cells were positioned at an angle of 45 degrees to capture the shear stresses.

It is not difficult to see that all gages will give an output signal for even the simplest applied load. This complex interaction will result in a highly nonlinear behavior on the output signal. This simple design of the hardware requires a very complex analytical method of calibration. We employed here a neural network calibration method. The software is trained from the strain fields exerted on the cell for each load applied and then gives a calibration mapping for the balance. We don't need to understand the non-linearity, since the code does it for us. For more information about the balance and its calibration, the reader may consult the paper by Vlachos *et al* (1999).

It is important to remark that even when available to be performed, the balance wasn't calibrated for this experiment, because the quantitative analysis is useless due to the high blockage present on the tunnel. The qualitative results are though compared just as output voltage magnitude variations, eliminating the need for calibration. A photograph of the finished balance is shown in Figure 4.3.4.2.

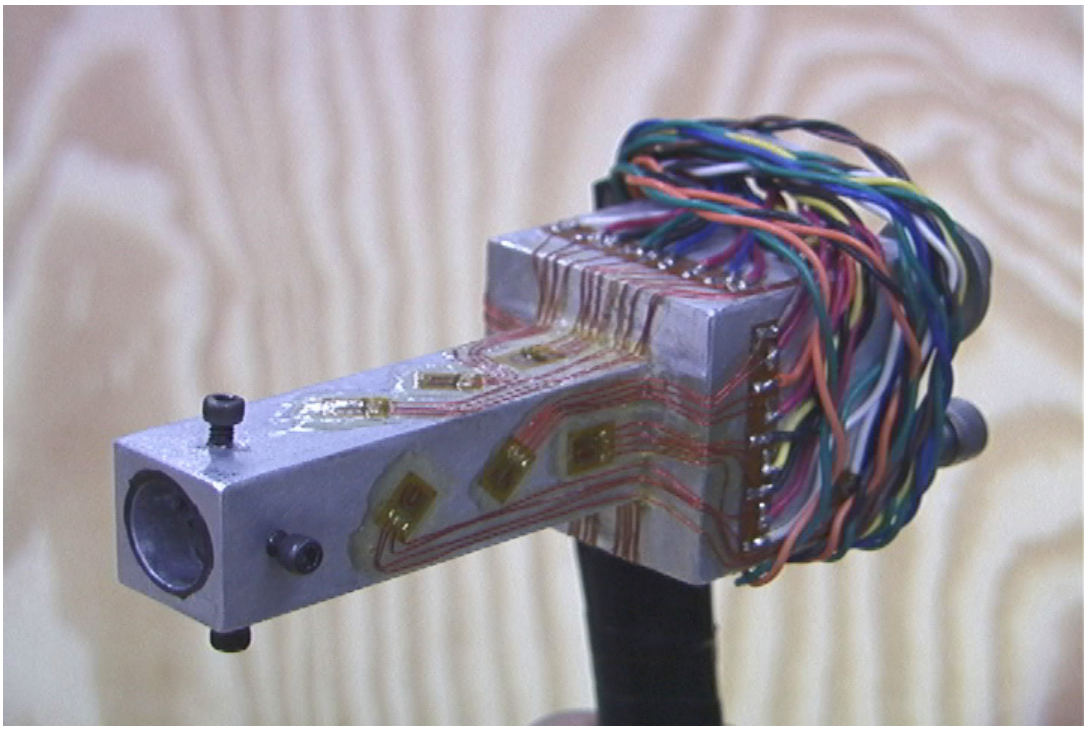

Figure 4.3.4.2 Strain gage balance

The connection of the balance to the wing model is shown in Figure 4.3.4.3. A 12.7 mm (1/2 ') aluminum rod is tightly inserted in the balance axial hole and secured with four setscrews. On the other side of the rod a universal joint links the balance system and the

airfoil structural shaft. The wing is supported on the other side of the wind tunnel by a mechanism that allows rotational movement on any of the axis but constrains linear displacements in any direction. The universal joint behaves in a similar fashion, constraining all displacements but two rotational ones. Figure 4.3.4.3 also shows the degrees of freedom on the universal joint and the wing support.

From the drawing, it can be concluded that only three components can be measured by the balance (and the ones we are interested on). Namely lift, drag and moment about the airfoil model axis. Figure 4.3.4.4 gives a close up view of the universal joint.

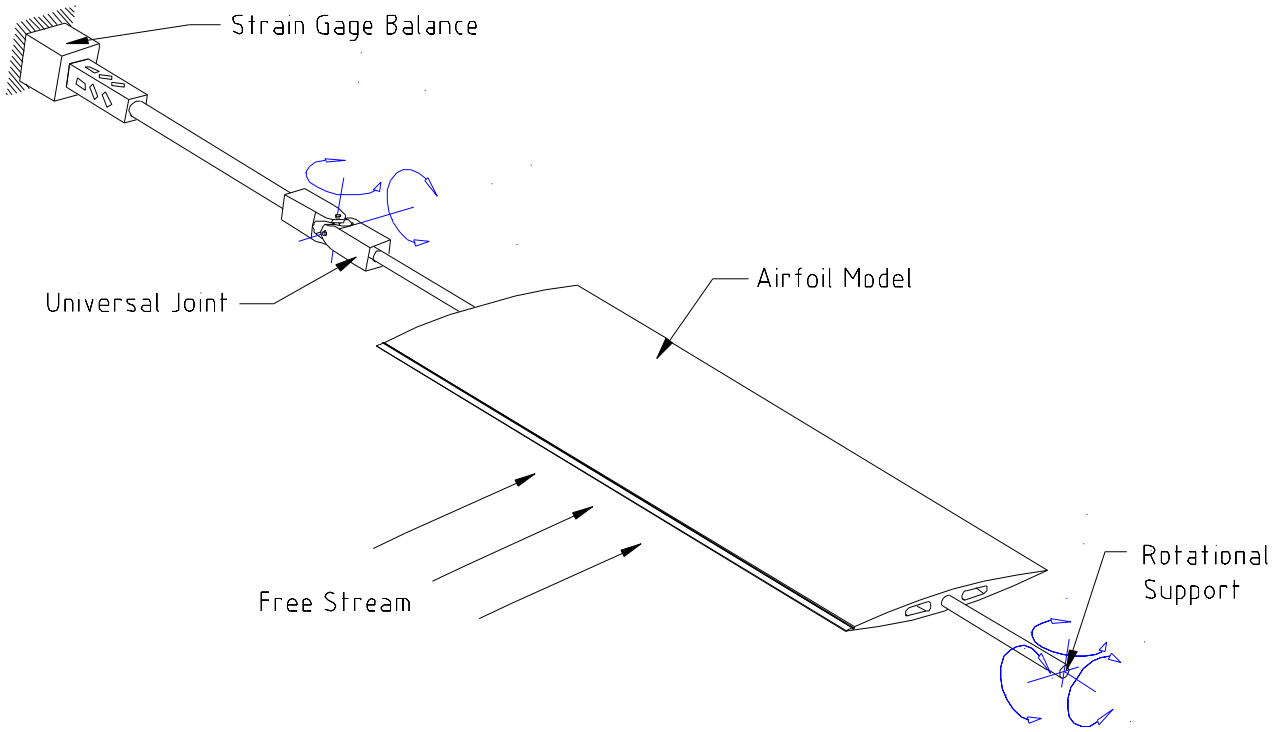

Figure 4.3.4.3 Balance/Wing system and degrees of freedom.

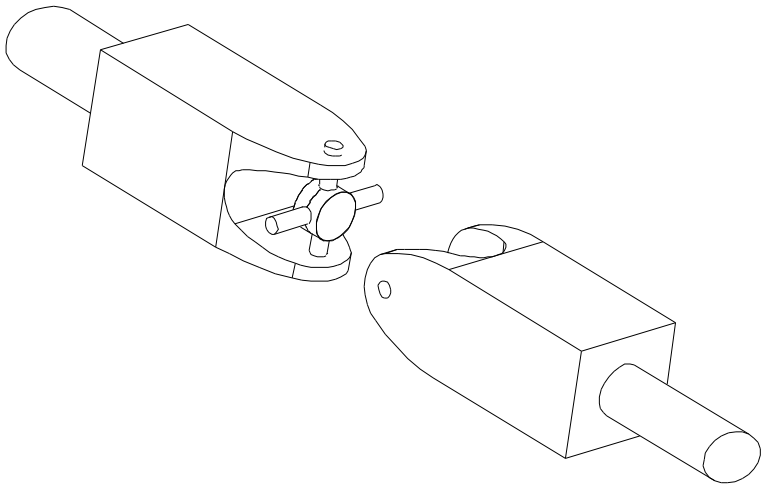

Figure 4.3.4.4 Universal joint exploded view.

4.3.5 Pitot Rake

As seen before, the most effective way of controlling the separated flow over the airfoil is by introducing disturbances with frequencies equal to the harmonics of the vortex shedding frequency. For this reason, a sensor is required to read a signal needed for the control. There are many ways to accomplish this task:

(a) Get the balance unsteady readings

(b) Place a pressure sensor near the stagnation point on the pressure side and check the pressure oscillation (i.e. Proportional to the lift due to the total circulation change around the wing)

(c) Place a velocity sensor on the wake of the airfoil reading directly the vortex induced pressure variations

The first method was eliminated from the beginning for the reason that the readings do not record directly the aerodynamic consequence effects over the wing, but also the aeroelastic response of the wing to these perturbations. This increases the complexity of the problem, and deviates from the original goal: base our attention to the flow characteristics only. For future aircraft application the latter is the desired goal, since a cheap strain gage sensor could be placed on different stations on the wing sensing the wing oscillations and applying a control law to the actuator to improve the flow over the wing surface. This is also a direct measure of the parameter we want to control. Of course,

this requires more effort and is going to be airframe dependent. We want to eliminate this dependency and focus our attention on the flow characteristics.

The second method is probably the better of the three possibilities, but the restricted space inside the wing wouldn't allow the placement of a sensor. Tubing would be necessary to direct the pressure readings outside the airfoil, and this definitely tampers with the frequency response of the sensor. The following question arises also: Why not measure directly on the suction side, where all the flow phenomena to control is taking place? The answer is simple: It is really difficult to predict the right position where to relate measured pressures to the vortex shedding. In the suction side, the flow topology is complicated to predict, and it's uncertain how to relate frequencies from pressure readings of the airfoil surface to the actual wake shedding frequency. At least, more research is necessary in order to implement this method.

This leaves us with the last possible method, and at the same time the simplest form to implement in a wind tunnel, where the vortex shedding process is directly acquired by a Pitot instrument, equipped with a high frequency pressure transducer placed on the wake of the airfoil. This is the least expected option to be used on an aircraft. Unless the tail lies on the wake of the wing, which is not desired from the design point of view, there is no way to place sensors behind the aircraft for obvious reasons.

This method was selected and a Pitot rake was constructed using high frequency response pressure transducers. The pressure transducers capture the already developed vortex street axial velocity variations in the wake of the airfoil, and the signals are digitally processed to obtain the required frequencies.

The rake was constructed using 6 total pressure Pitot tubes, containing high frequency Endevco Model 8510B-2 piezoelectric pressure transducers having a 2 psig full range. The adjustable characteristic of each Pitot tube led to a correct placement of each sensor on the wake. The Pitot tubes are made from bronze tubing and each of them connected to a Plexiglas block machined to contain the pressure sensors. Each block was positioned on a traversing guide allowing the manual adjustment of the sensors along the wind tunnel section. An aerodynamic fairing covered the resulting structure reducing the interference and power losses. The schematic drawing of the rake and Pitot numbering can be seen in Figure 4.3.5.1. Figure 4.3.5.2 shows a picture of the finished rake.

The static reference pressure on the Endevco's was taken from the static port on the wind tunnel's pitot tube. Before the installation on the rake, a full calibration of the six Endevco's was performed in the estimated pressure range to be used.

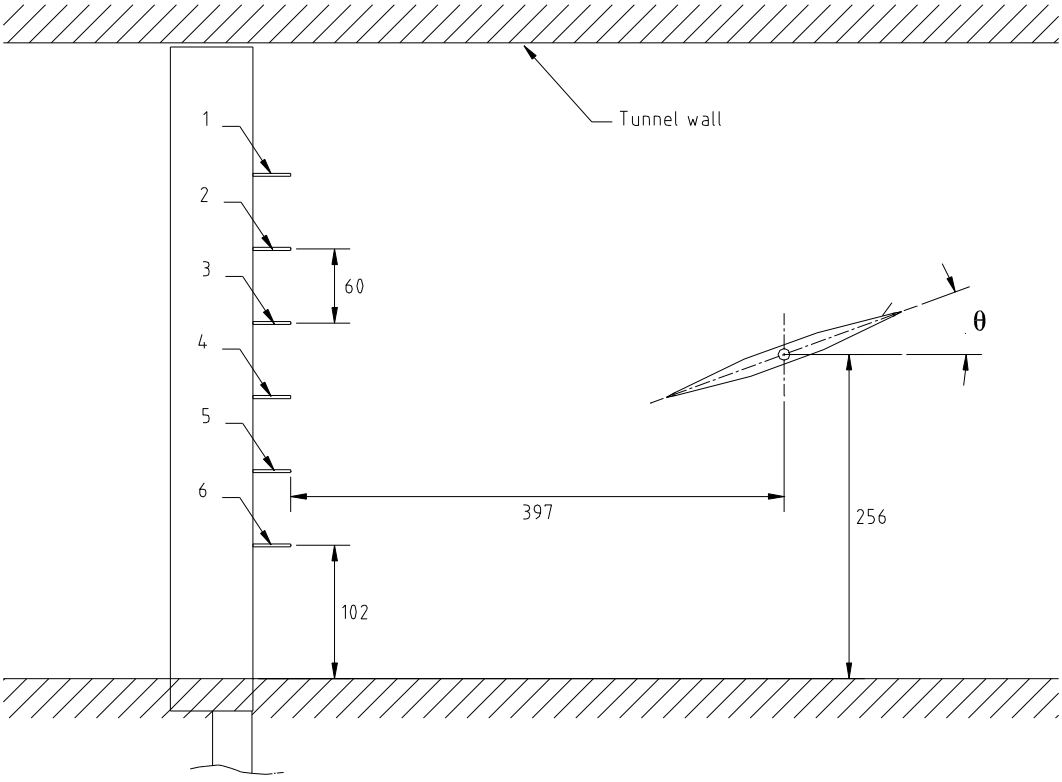

Figure 4.3.5.1 Pitot Rake Positioning

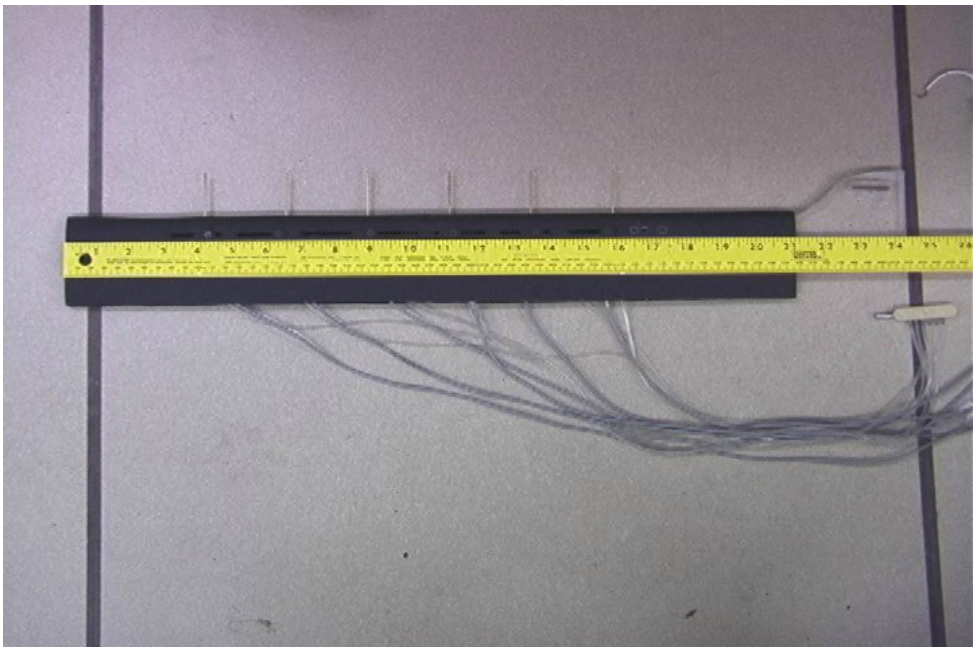

Figure 4.3.5.2 Pitot Rake

4.4 Data Acquisition System and Additional Instrumentation

The equipment previously described needs an acquisition system that conditions and amplifies the signals and then converts to digital format for latter analysis. This task is performed on this experiment through different equipment. Four signal conditioning amplifiers are used, and the data are acquired by means of two acquisition boards on two computers. A schematic diagram is shown in Figure 4.4.1 that summarizes the complete acquisition system set up. For the analog signal coming from the PSD, the company's OT-300 position sensing amplifier is used. A BNC connector on the amplifier provides an analogous ±10 Volts full scale output signal.

Signals from the six Endevcos are amplified and conditioned by Vishay Measurements Group Inc., Instrument Division, Signal Conditioning Amplifier Model 2210. The six strain gage channels are amplified by Vishay Measurements Group Inc., Instruments Division, Signal Conditioning Amplifier Model 2120A.

For the multiplexed signal coming from the ESP, Aeroprobe's AP-2500 Box is utilized.

Two computers are employed for simultaneous data acquisition of airfoil pressure distribution, balance forces, and pitot rake survey. Both computers are triggered externally through a simple LOW-HIGH triggering signal coming from a function generator.

Computer I runs under a 166 MHz Intel Pentium processor and 32 MB of RAM memory. A RC electronics ISC-16 acquisition board makes the analog to digital conversion of the signal coming from the devices. The ISC-16 is a 16 channel, 12 Bit, ±10 Volts range, capable of up to 1 MHz maximum rate. The six channels from the pitot rake, plus the six additional channels from the strain gage balance and the channel coming from the PSD conform the thirteen total channels utilized on the ISC-16. The acquisition program used in computer I is a modified version of the C coded program created by Schaeffler (1998). The program was modified in order to customize it for the experiment.

The Hewlet-Packard HP-3562A Dynamic Signal Analyzer is an important tool for the data acquisition process. Two channels are available for real time analysis of signals. It not only has functions attributed to oscilloscopes but also works as a real time digital signal processor, showing power spectrum densities, correlation, etc. This is a fundamental feedback tool to control and modify the vortex shedding phenomena, adjusting the actuator frequency, and observing changes in forces exerted on the balance. This reduces post-processing time by getting a real time feedback of the physics of the experiment.

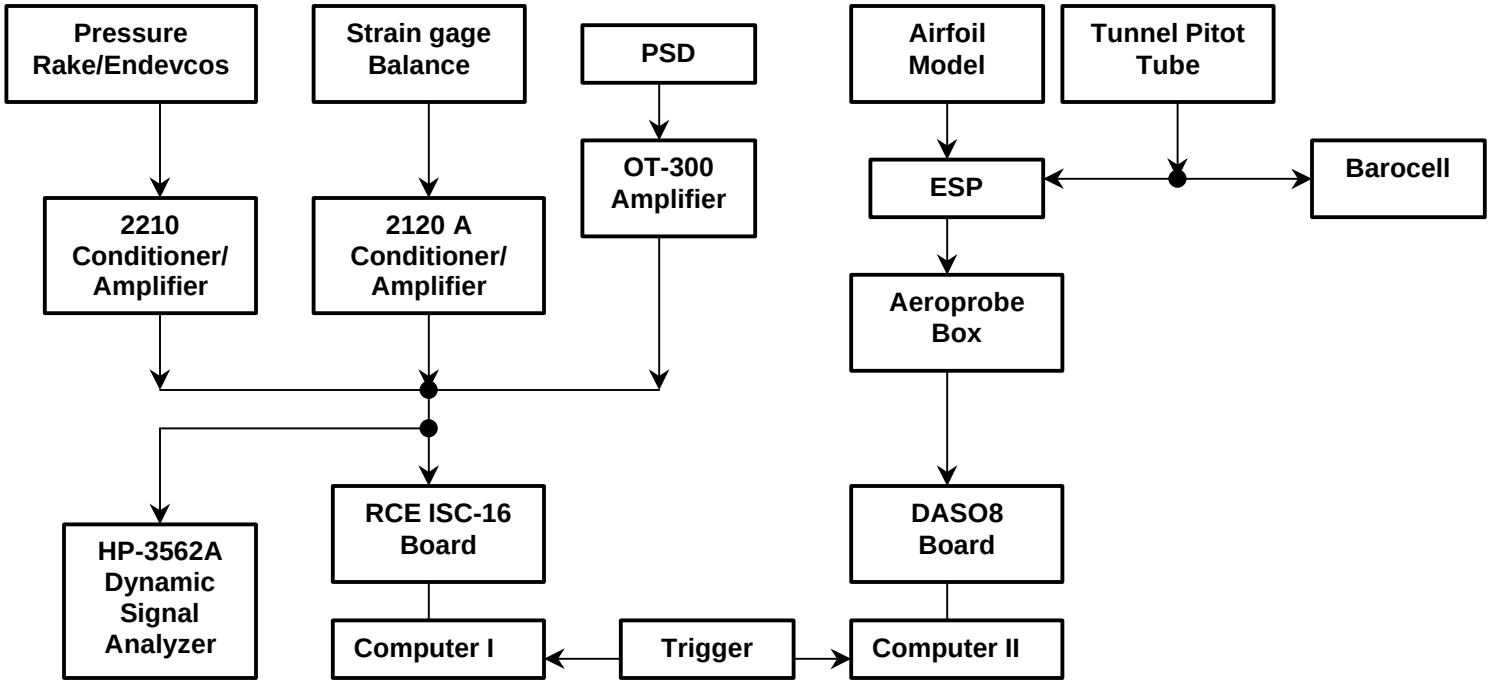

Figure 4.4.1 Schematic diagram of the experimental set up

Computer II runs under a 166 MHz Intel Pentium Processor and 4 MB of RAM memory. The data acquisition board is a Computer Boards model CIO-DASO8-AOL, being an 8 channel, 20 kHz, programmable gain, 12 Bit Analog to Digital converter and 2 channel 12 Bit Digital to Analog converter. Computer II is the platform for the Aeroprobe's pressure measurement system. Proprietary software is utilized which controls all the required parameters on the ESP for data acquisition and its calibration. The program is set for an external trigger, as done for Computer I.

It's important to note from the Figure 4.4.1 that the Edwards-Datametrics Barocell precision pressure transducer, and the Pressure Systems Incorporated ESP are both connected to each other and to the tunnel's freestream Pitot tube. The Barocell conforms the actual pressure to velocity conversion reading necessary to adjust the tunnel freestream velocity. It also takes part in the ESP static calibration, measuring the calibration pressures. The ESP is calibrated every 20 minutes, to maintain the required accuracy on the measurements. The reference static pressure of the ESP on the run mode is taken from the static port of the Pitot tube. The last channel on the ESP is connected to the total pressure port of the tunnel Pitot tube, recording the freestream velocity. For detailed information about ESP calibration and data acquisition procedure, programs, and system limitations, the reader is referred to Schaeffler (1998).

Chapter 5 Experimental Results

5.1 Rake Calibration and Positioning

Before starting the experiment, it was necessary to confirm that the built-in rake was performing as desired. Since the shedding frequency is the most important parameter for the feedback control, the correct frequency reading on the Endevco's had to be assured. For this reason, a simple yet effective method was utilized: measure the shedding frequency emanating from a circular cylinder. Several investigators had already extensively analyzed this unsteady process and large amount of data are available for comparison. A circular 55.6 mm diameter cylinder was placed in the wind tunnel test section and the rake positioned in its wake. The rake was placed in the wind tunnel longitudinal axis. This is shown in Figure 5.1.1.

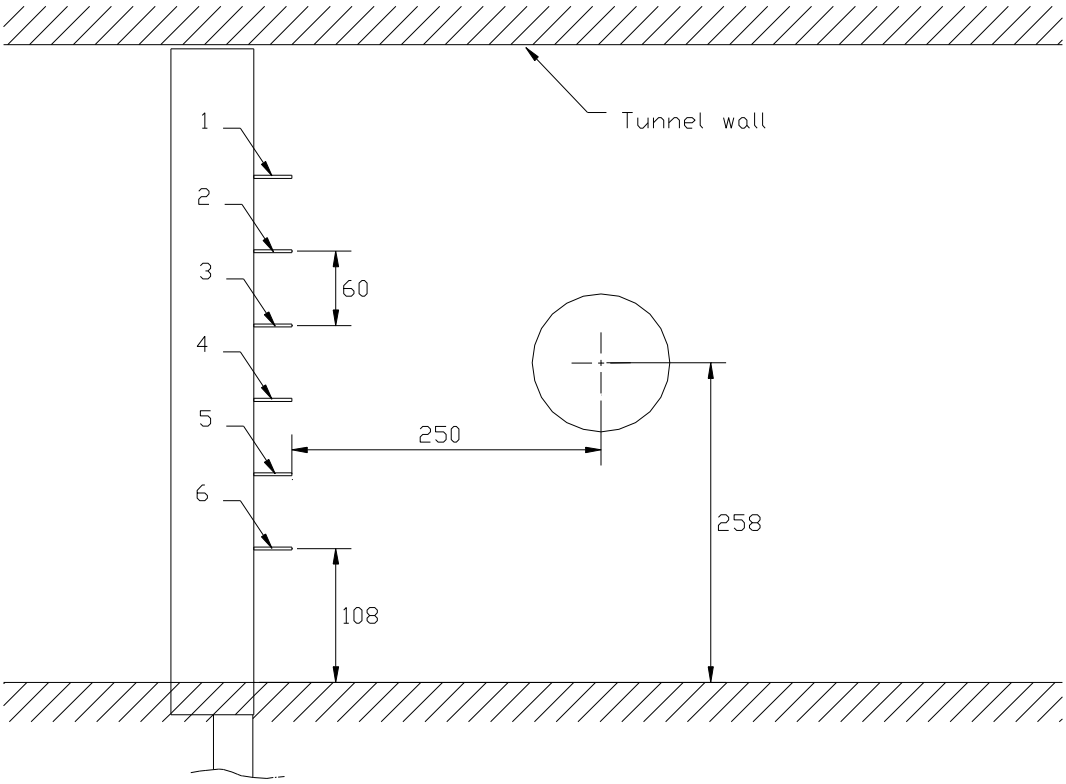

Figure 5.1.1 Circular cylinder positioning for rake calibration

After the cylinder and rake where securely attached in the tunnel, seven different tunnel speeds where tested and the Endevco's output signal obtained. For this case, the computer I acquisition program was set for a sampling frequency of 512 Hz and a sampling time of 4 seconds.

Wind tunnel velocities ranged from 6 to 16 m/sec, and at intervals of around 2 m/sec. Figure 5.1.2 shows the frequency spectrum for the different pitot tubes for the highest speed case, 16.2 m/sec, corresponding to a Reynolds number of 52590. It can be seen that all the Endevco's can capture the fundamental shedding frequency, at a different order of magnitude. Pitot 4 shows to be the most sensitive one, and this behavior is observed for all wind tunnel speeds tested.

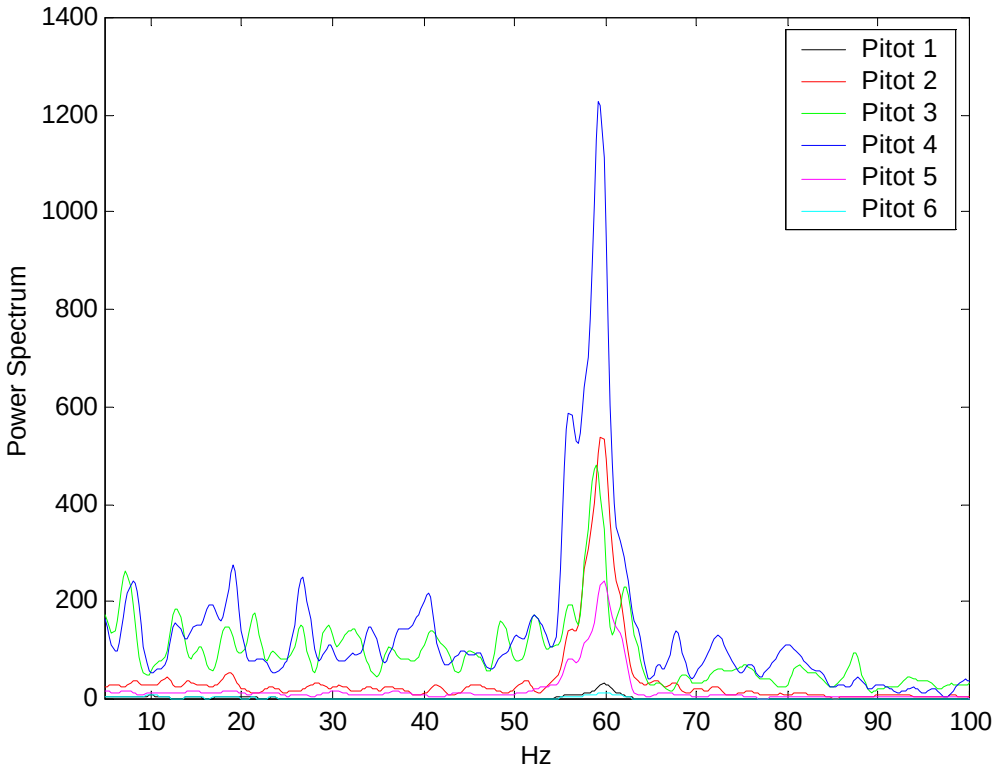

Figure 5.1.2 Frequency spectrum on the rake for V_∞= 16.2 m/sec

Taking pitot 4 as the reference for the calculations, data obtained were compared to the work of Roshko (1954) who carried out a semiempirical study of the vortex shedding from cylinders. The experiments were performed in the 20 by 20 inch low turbulence wind

tunnel at GALCIT. This is exactly the same test section at the ESM tunnel where the rake was tested.

Data available from two circular cylinders tested, one having a diameter d(1) = 22.2 mm and the other d(2) = 6.38 mm, was used for the comparison. This is shown in Figure 5.1.3.

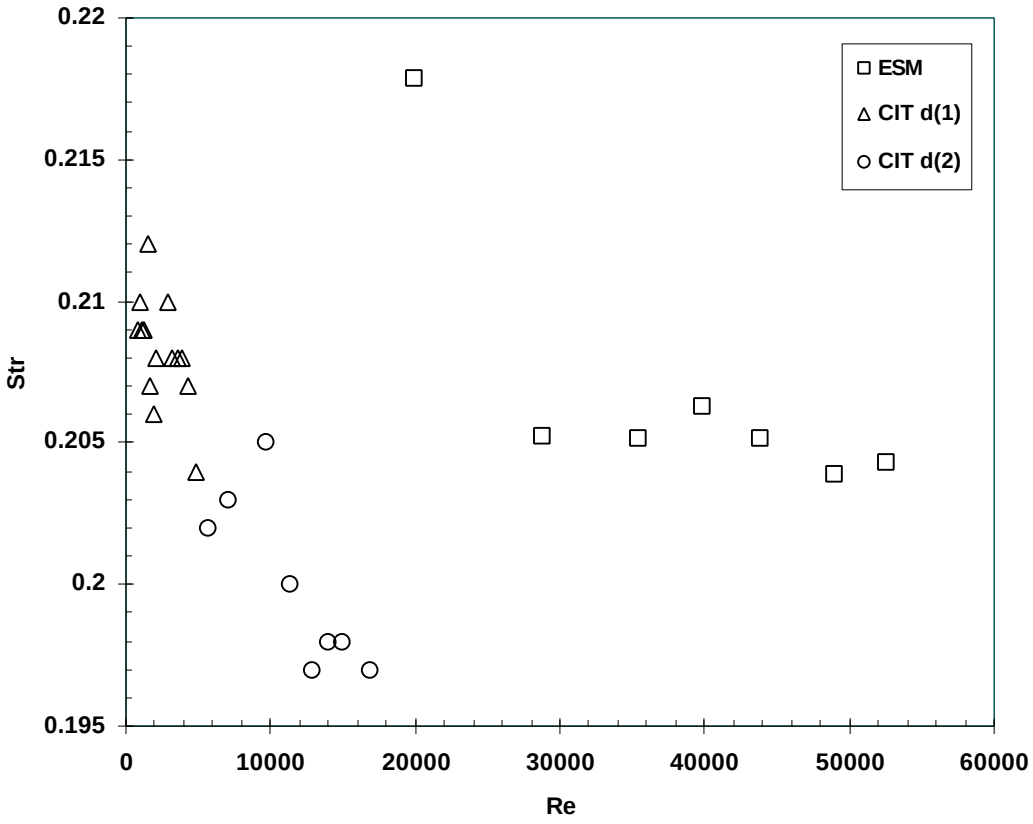

Figure 5.1.3 Comparison of results for circular cylinder vortex shedding

Even when the experiments where performed at different Reynolds numbers, a good correlation was found. It must be noticed that the deviation of the lowest Reynolds number case obtained in the ESM tunnel, can be attributed to both the turbulence level of the tunnel and to the low total pressure level in the tunnel for the Endevco's full range.

Once the rake performance was tested, the circular cylinder was removed and the airfoil model placed on the test section. The positioning of the rake is critical in the sense that a fully developed wake is desired to measure the shedding frequency. The optimum position will result from a compromise between a developed flow and a fully turbulent one. We do not want the vortices to break down completely and convert to turbulent eddies.

The maximum downstream position was also limited physically by the test section length. The rake was first placed at the furthest position from the model. A simple and effective way to see if the distance was appropiatte, was through fluid visualization. A Martin smoke generator was used and the smoke inserted directly through the wind tunnel intake. A 1000 W halogen lamp created a light sheet on the airfoil wake street, and a Sony DCR-TRV900 Digital Video Camera recorded the unsteady flow field on the wake at 30 frames per second and with an image definition of 640 by 480 pixels. This visualization was performed with the old airfoil model, but since the model dimensions were reproduced on the improved one, any contribution from the test was useful for the latter.

A sequence of the vortex shedding is shown in Figure 5.1.4 for 30 and 50 degrees angle of attack. It can be clearly seen that the vortex shedding is captured with the rake, and no adjustments were needed on the distance from the model nor the separation between pitot tubes. For lower angles of attack, since the vortex street is reduced in height, the Pitot tubes should be repositioned using the rake's adjustable feature, to cover more points on the area of interest (wake).

Drawing and dimensions of the final position of the rake and airfoil are shown in chapter 4 in Figure 4.3.5.1.

5.2 Data Acquisition Process

The data acquisition process is divided in two branches: pressure measurements and force measurements. The latter case can include pressure acquisition to check how the aerolastic behavior of the airfoil model affects the flow field. Since the balance still needs more research time in order to be used as a measuring tool, we will focus our attention to the measurement of pressures and dedicate a special section to the results obtained with the balance. In order to do this correctly, the balance was clamped to avoid any unsteady flow generated oscillation of the airfoil model.

The method of excitation of the shear layer was divided in two parts: perturbation of the leading edge shear layer, and perturbation of the trailing edge shear layer. Both methods use the same flap set up (i.e.: the same flap). The difference lies in the rotation of the airfoil by an angle of (180 – 2 α) degrees from the desired angle of attack. The schematics of this change can be seen in Figure 5.2.1.

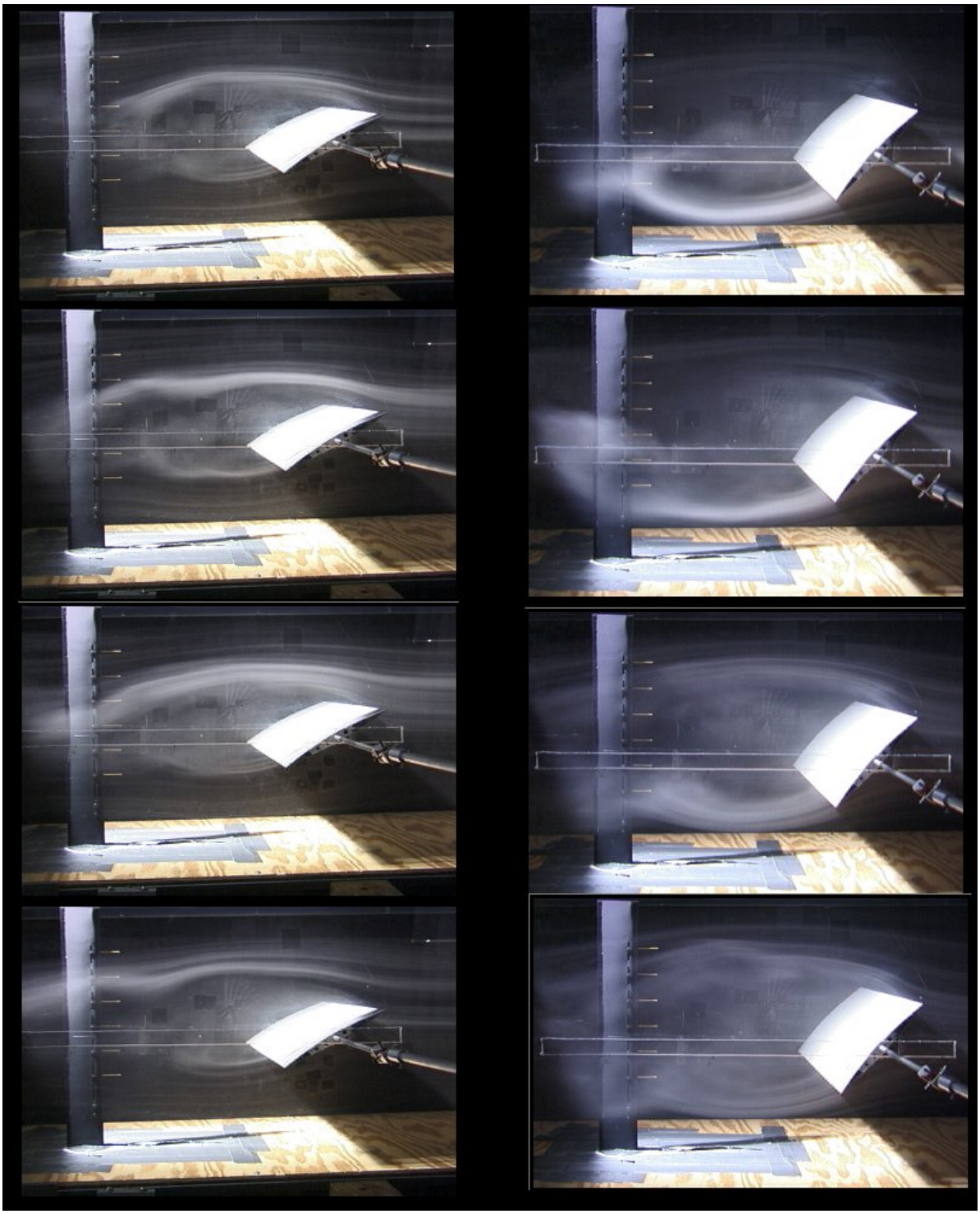

a) **b)**

Figure 5.1.4 Vortex shedding visualization for rake alignment, $U_\infty = 6.5\ m/s$;a) Angle of attack 50°, b) Angle of attack 30°.

The flap in both cases is located on the suction surface of the airfoil, and the moving sharp-edge face the leading/trailing edge. If both vortex-vortex and sound-vortex resonance is present, this should be the best configuration, as advised in the paper by Wu *et al* (1991)

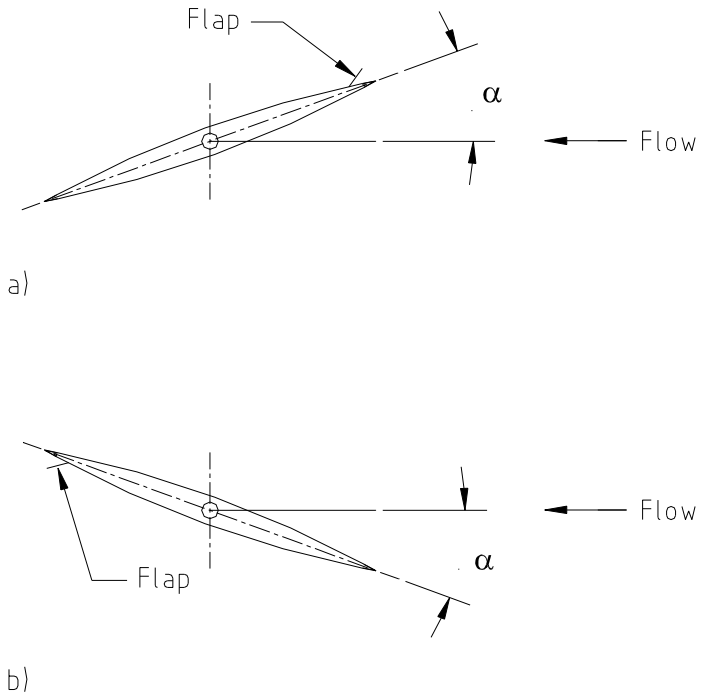

Figure 5.2.1 Schematic of flap positions tested. a) Leading edge flap; b) trailing edge flap.

This research is a parametric study of the effects of the flap actuation for different angles of attack. The following procedure was adopted:

I. Set the desired angle of attack.
II. Set the freestream velocity.
III. Using the dynamic signal analyzer, check the natural shedding frequency.
IV. Acquire data, no actuation applied.
V. Set excitation frequency.
VI. Acquire data with actuation.

It can be seen that this implies an iterative process. Steps V and VI are repeated until all possible/desired excitation frequencies are covered (flap physical limitations restricted the actuation from 10 Hz to 110 Hz). When the frequencies are exhausted, two options were available: repeat parts of the experiment after completely shutting off the tunnel to check the repetition of the results, or change the angle of attack and start a new loop. It's important to notice that calibrations were performed regularly to maintain a good level of accuracy in the measurements.

A comment should be added at this stage: the freestream velocities chosen were a mere compromise between the pressure voltage readings on the ESP and the natural vortex shedding frequency evolving on the airfoil wake. The former affects the precision on the measurements due to the pressure range and accuracy of the ESP, and also the small error of the data acquisition card. The latter is directly linked to the flap frequency limitations and the desired frequency range to be covered: the subharmonic and harmonics of the shedding frequency are to be experimented. Also the tunnel motor posed a limit on the maximum speed possible to be reached: a big blockage is present at high angles of attack, requiring a bigger power for the same freestream speed.

A summary of the adopted speeds for given angles of attack is shown in table 5.2.1. The table also reflects the Reynolds numbers range at which the cases where tested, and the type of excitation configuration used. Blockage percentage is also included in order to show the conditions present on the test section.

Tunnel corrections as the ones given in Barlow *et al* (1999) are practically useless due to the conditions existing in the experiment. By no means, the results were expected to correlate quantitatively to any previous in the literature. Only qualitative data are required in order to confirm the efficiency of the excitation system, and prove that a more realistic experiment should be performed. The purpose of this experiment was to prove the basic concept and also to provide the guidelines for more experiments at higher Reynolds numbers and with a larger number of diagnostic tools.

Thirty two channels are available on the ESP pressure scanner, and 61 pressure taps on the airfoil surface. A defective port was found on the ESP, making the total available number of ports equal to 31. Since one port is used to read the tunnel free stream velocity, this leaves us with 30 ports to be distributed over the airfoil.

The optimal distribution of the available channels was found by tracking the pressure distribution for some cases, by performing measurements using all pressure taps either on the pressure side or the suction side at a time. By looking at the pressure

characteristics over the airfoil, an optimum pressure tap utilization that reflects the particular flow field for each case was selected as depicted in Figure 5.2.2. Table 5.2.2 gives the location of the pressure taps in the airfoil.

Angle of attack	*Freestream Velocity [m/sec]*	*Reynolds Number [x10^5]*	*Excitation Configuration*	*Tunnel Blockage*
10°	**17.5**	**2.22**	**LE**	**6.9%**
15°	**17.5**	**2.22**	**LE**	**10.3%**
20°	**17.5**	**2.22**	**LE/TE**	**13.7%**
25°	**17**	**2.16**	**LE**	**16.9%**
30°	**17**	**2.16**	**LE/TE**	**20%**
40°	**15.5**	**1.97**	**LE/TE**	**25.7%**

Table 5.2.1. Experiment parameters on the airfoil testing. LE: leading edge; TE: trailing edge

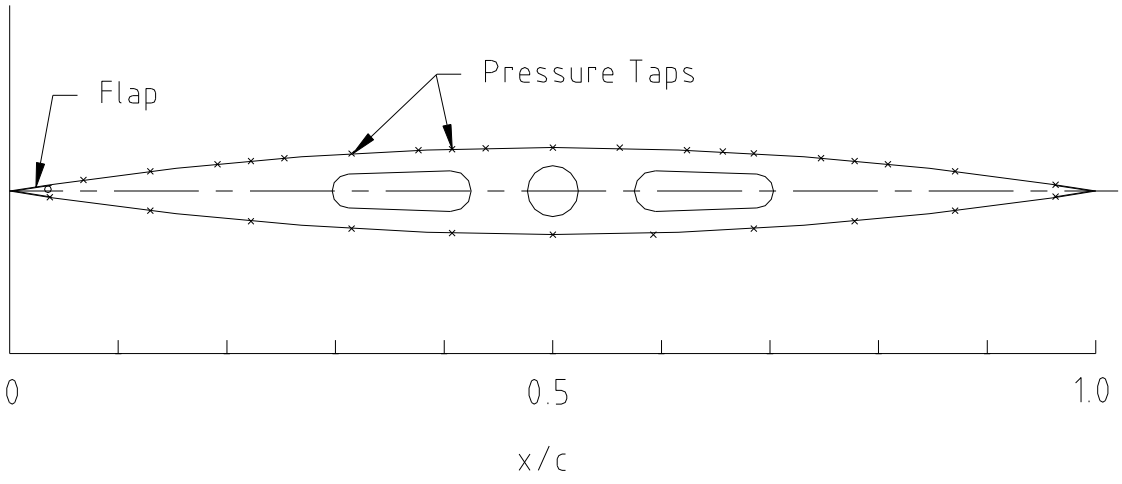

Figure 5.2.2 Pressure taps measured in the experiment.

x/c Upper Surface	*x/c Lower Surface*
0.0696	***0.0389***
0.1311	***0.1311***
0.1926	***0.2234***
0.2234	***0.3156***
0.2541	***0.4078***
0.3156	***0.5000***
0.3771	***0.5923***
0.4078	***0.6845***
0.4386	***0.7767***
0.5000	***0.8690***
0.5615	***0.9612***
0.6230	
0.6538	
0.6845	
0.7460	
0.7767	
0.8075	
0.8690	
0.9612	

Table 5.2.2 Pressure taps location

A comment should be made on the parameters selected on the data acquisition programs for computers one and two. Taking into account the sampling theorem, the minimum required Nyquist sampling rate is twice the maximum acquired frequency. In practice, around five times the maximum experiment frequency is recommended to obtain a good reconstruction of the signal. Since the ESP maximum frequency response is of 50 Hz without tubing damping (Schaeffler,1998), a sampling rate of 256 Hz with a sampling time of 4 seconds were selected for computer two. In computer one, achievable maximum flap frequencies are in the order of 100 Hz, and expected shedding frequencies do not exceed those values. Therefore, a sampling rate of 512 Hz was chosen, acquiring data also for 4 seconds.

5.3 Results

5.3.1 Base flow

In order to understand the fluid dynamics of the circular-arc airfoil at high angles of attack, results with no excitation are analyzed first. These are also the basis for the comparison with the controlled cases.

Pressure measurements taken from the surface of the airfoil can be converted to pressure coefficients by virtue of the formula:

$$C_p = \frac{P - P_\infty}{\frac{1}{2} r U_\infty^2}$$

Due to the natural unsteadiness present in the flow over the airfoil, a simple time-average can be taken over the data obtained. The averaged values are displayed in Figure 5.3.1.1 for different angles of attack. It is important to note that a sensor malfunction is found in the port placed at the 62.3% of the chord on the suction side. A clear constant offset out of the normal error margins is encountered for all cases.

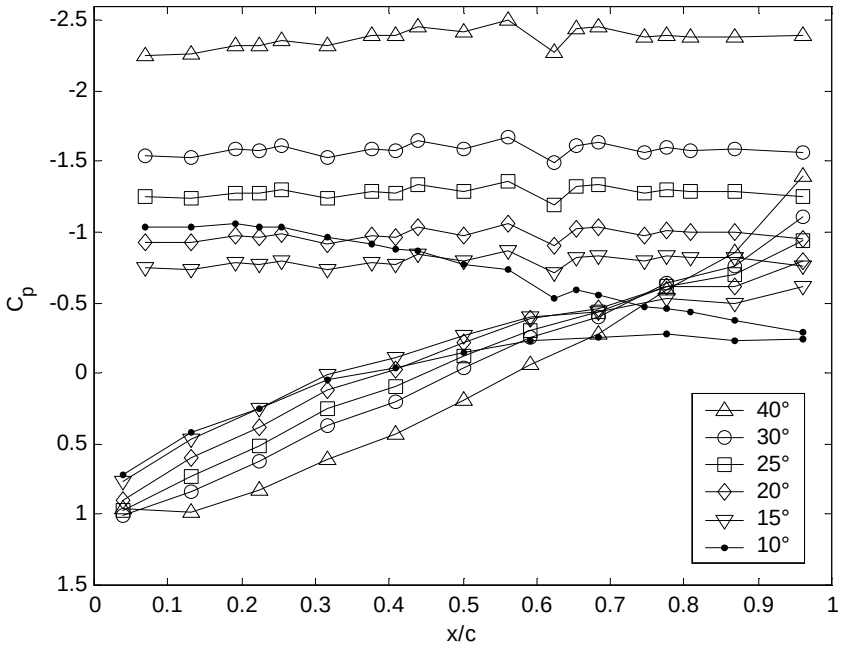

Figure 5.3.1.1 Airfoil pressure coefficient distribution at different angles of attack. Suction and pressure sides. No actuation. For Reynolds number, see Table 5.2.1.

The figure shows that a flat top average pressure distribution, characteristic of completely separated flows is present for all angles of attack, except the case of 10 degrees. This correlates with the idea of the flow around a sharp edged airfoil: separation is inevitable at the edge and reattachment is not possible unless the airfoil is at low angles of attack. The flow physics behavior encountered is then that of a bluff body.

The stagnation point is very near to the leading edge except for the highest angle of attack. The point moves towards the leading edge as incidence is decreased, and practically lies at the edge for the lower angle s. This, and the fact of the low Reynolds number testing, makes us think that the separation on the leading edge of the airfoil is completely laminar. Since the laminar shear layer is natural unstable, transition occurs, and reattachment is only possible if the airfoil wall is close to the shear layer. That's probably the physics behind the 10 degrees case; a thickening of the shear layer due to transition to turbulence brings the fluid back to the airfoil wall, reattaching and forming a favorable flow recirculating region. If the angle of attack is increased, the reattachment point moves forward, until it reaches the trailing edge, were the airfoil completely stalls. Once the stall condition is found, vortex shedding starts to occur.

Readings from the Pitot rake could clarify this process. Before analyzing the acquired data for different angles of attack, it is important to search for the Pitot tube that is more sensitive to vortex shedding in the configured rake. Figures 5.3.1.2 and 5.3.1.3 present the power spectrum density (PSD) of the pressure readings for the different sensors in the rake. The case selected is 20° angle of attack, and the PSD is performed over the data in Pascals.

It is clear that all the sensors in the rake can capture the fundamental frequency of the vortices shedding from the airfoil. A peak is present for this case in 56 Hz. The same behavior is found at different angles of attack, and port 3 is selected as the point of comparison. The effect of change of angles of attack on the vortex shedding characteristics is represented in Figure 5.3.1.4 and 5.3.1.5.

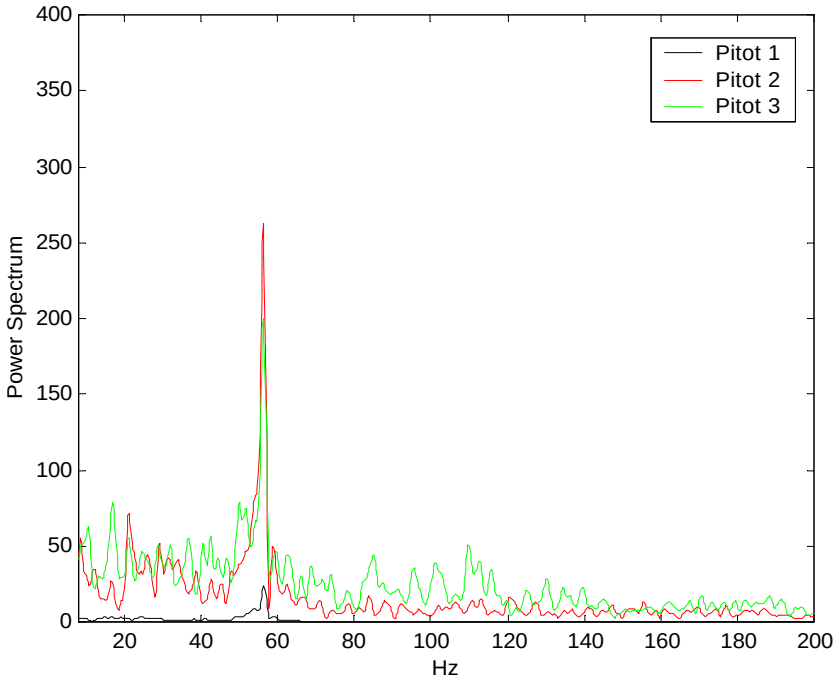

Figure 5.3.1.2 Power spectrum density on the rake for pitots 1 through 3. Angle of attack 20°. $U_\infty = 17.5\ m/s$

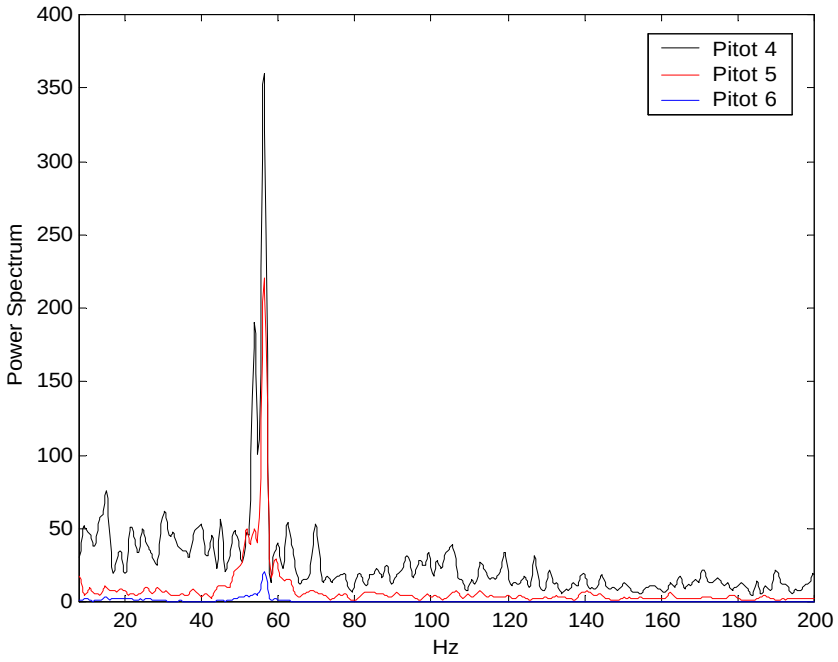

Figure 5.3.1.3 Power spectrum density on the rake for pitots 4 through 6. Angle of attack 20°. $U_\infty = 17.5\ m/s$

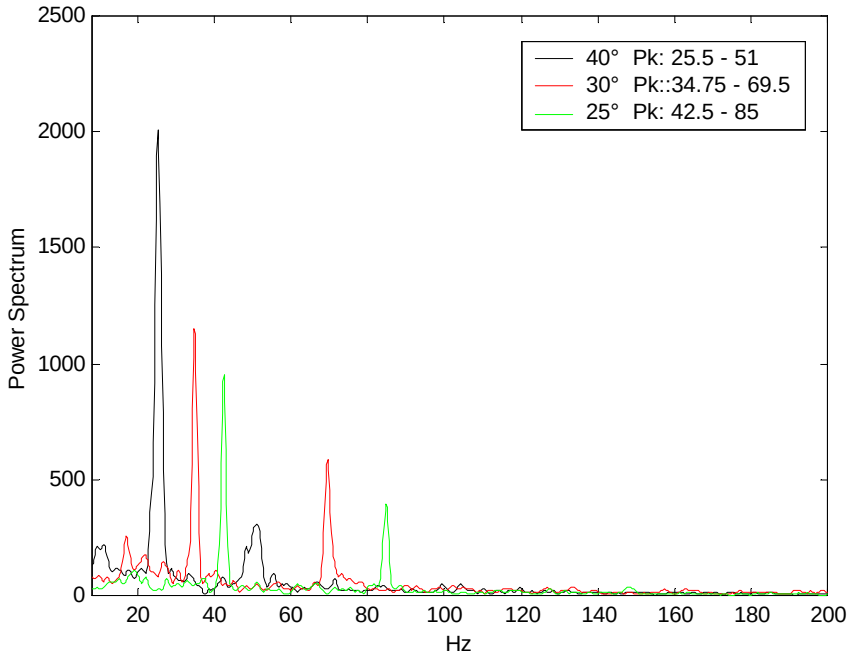

Figure 5.3.1.4 PSD at angles 40° through 25°. Pitot 3. Reynolds number and freestream velocity as in Table 5.2.1. PK: peak values.

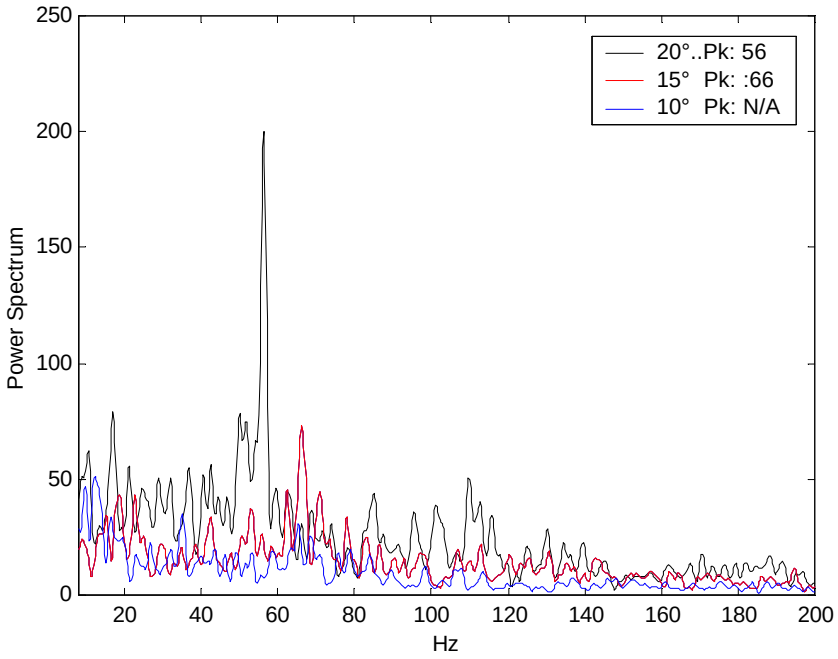

Figure 5.3.1.5 PSD at angles 20° through 10°. Pitot 3. Reynolds number and freestream velocity as in Table 5.2.1. PK: peak values.

The vortical structure in the wake is characterized by two frequencies, a shedding frequency, and also a component at the first harmonic. This is true for the high angles, whereas the second component reduces in magnitude as angle of attack diminishes. For the 20° case, practically only one component is present. This means that a more organized vortical flow is present for the higher angles, where two strong vortices coexist and shed periodically, a result of the global nonlinear interaction of the leading and trailing edge vortex layer roll up.

The 15° case shows a less clear peak on the PSD plot, corresponding to a less organized flow. This could also imply that the flow is separated in the average, but a transient reattachment could exist due to the unsteadyness of the flowfield. That means that a recirculating bubble is formed, but its unstable characteristics makes it burst and periodically shed away from the airfoil.

For the 10° case, a peak is not clear, and reflects the stable stationary characteristics of the recirculating bubble located in the suction surface.

Using the principal vortex shedding frequency, the Strouhal number can be computed based on the frontal height of the airfoil, yielding:

$$Str = \frac{f_s \, c \sin a}{U_a}$$

This number was found to be between 0.2 and 0.22 for all angles of attack greater than 10°. Assuming the same Strouhal number, the shedding frequency for the 10° angle of attack should be in the neighborhood of 100 to 110 Hz.

The unsteadiness associated with the flow around the circular-arc airfoil can be examined by presenting the evolution of the section normal force coefficient with respect to time. The normal force coefficient is calculated numerically integrating over the chord the unsteady pressure measurements taken over the surface the airfoil:

$$C_n = \int_0^1 \left(Cp_{suc} - Cp_{pres} \right) d\left(x/c \right)$$

The numerical integration is performed using the trapezoidal rule, and the limits of integration are reduced to the measured pressure area covered by the pressure taps. This

was done in order to avoid the use of extrapolation functions to calculate the pressure near the edges of the airfoil.

Figure 5.3.1.6 clearly exposes the periodic character of the flow over the airfoil at different angles of attack.

The most remarkable feature, is the amplitude of the pressure oscillations exerted on the airfoil at high angles of attack. At the same time, even when the magnitude of the oscillations increases, the pattern is more periodic, that is, more coherent. That's exactly what was observed from the PSD plots. At high angles of attack the vortex structure is more organized, with bigger vortices shedding in a more organized fashion.

In the lower-angle of attack regime, it is more difficult at first to observe a periodic behavior.

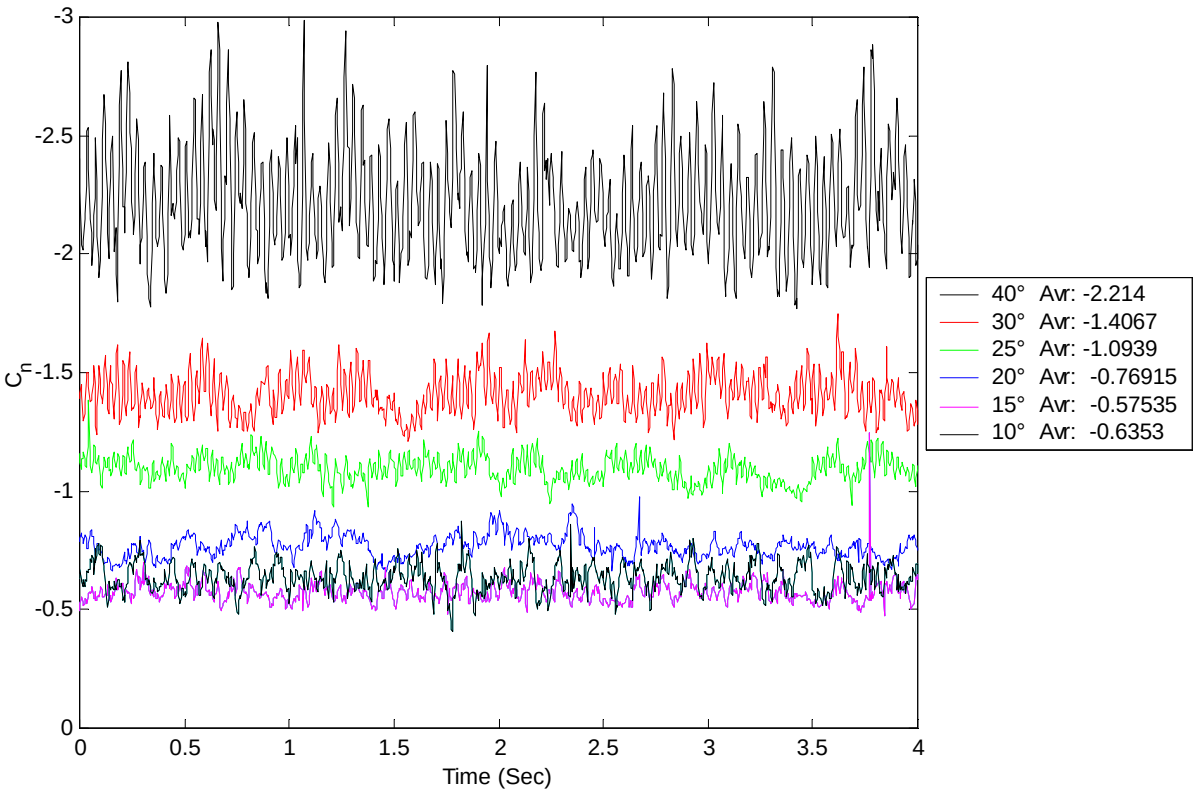

Figure 5.3.1.6 Base flow normal force coefficient with respect to time at different angles of attack. Freestream velocity and Reynolds number from Table 5.2.1. Avr: average value.

It is also not difficult to understand the need for flow control even at relatively low angles of attack. Since pressure fluctuations traduce to buffeting loads applied on the

structure, at normal aircraft dynamic pressures this exerted forces are considerable in magnitude.

After reviewing the basic characteristics of the base flow, we are able now to analyze the effects of excitation on the flow field around the airfoil.

5.3.2 Controlled Case

As previously mentioned, the data for different excitations were acquired by applying an excitation frequency and taking into account the shedding frequencies present for each angle of attack and freestream velocity. All data, were post-processed and compared with respect to the base case for each respective angle of attack. In this form, we can relatively compare the effects of the excitation on the flow field. Since flow over a sharp-edged bluff body maintains a small dependency on the Reynolds number, the effects can be extrapolated to engineering practical configurations.

Both normal force coefficient and Strouhal number are calculated for the different excitation cases and normalized with respect to the base case, being called |Cn| and |Str| respectively (|| means normalized value). The results are plotted with respect to the reduced frequency F for each angle of attack. This is shown in Figures 5.3.2.1 through 5.3.2.12. Since no vortex shedding is visible for the 10° case, the base case shedding frequency is given a unitary value in order to compute the Strouhal number and reduced frequency (i.e. showing the non-normalized values). This strategy will become clear eventually.

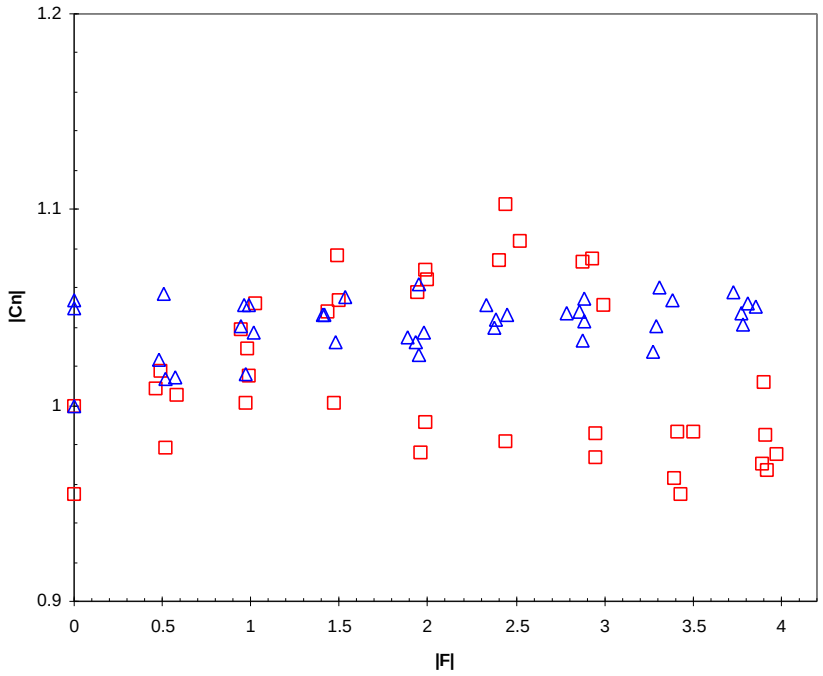

Figure 5.3.2.1 Normal force coefficient variation with excitation frequency. Angle of attack: 40°; □ leading edge flap actuation; △ trailing edge flap actuation.

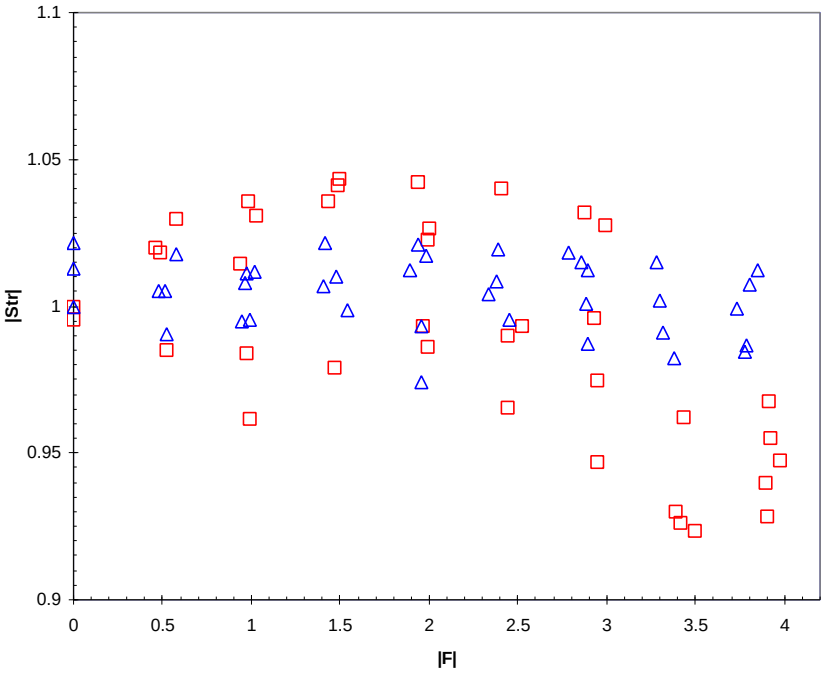

Figure 5.3.2.2 Strouhal number variation with excitation frequency. Angle of attack: 40°; □ leading edge flap actuation; △ trailing edge flap actuation.

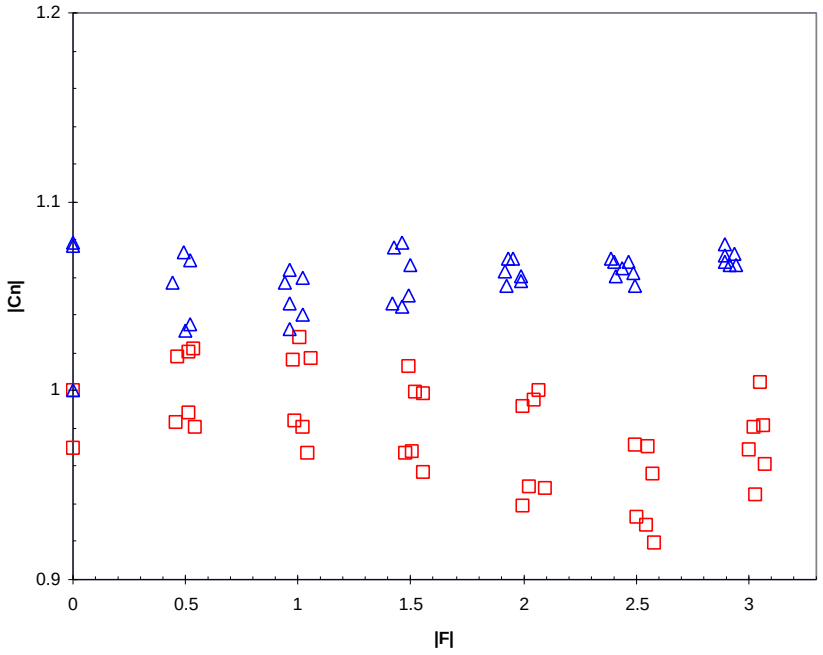

Figure 5.3.2.3 Normal force coefficient variation with excitation frequency. Angle of attack: 30°; □ leading edge flap actuation; △ trailing edge flap actuation.

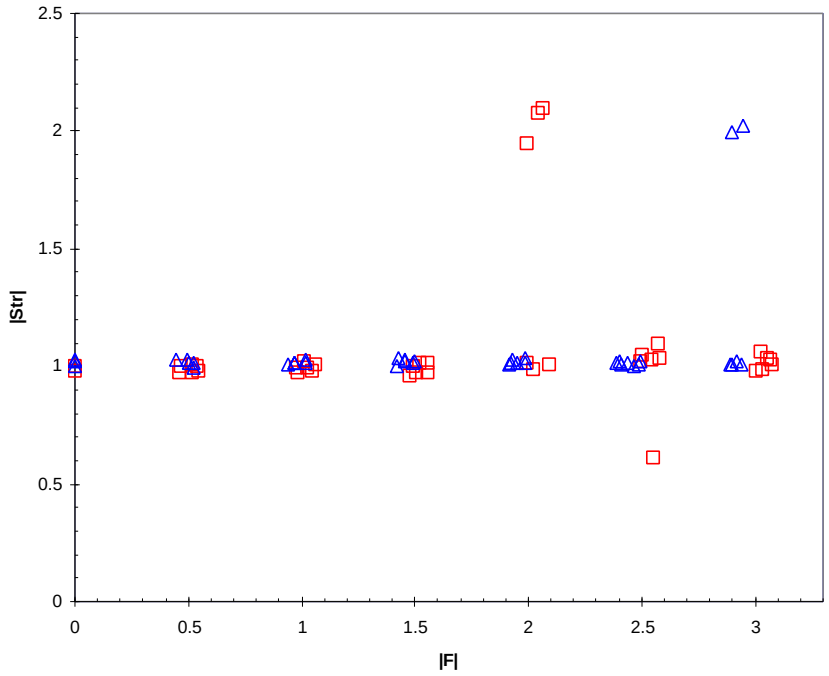

Figure 5.3.2.4 Strouhal number variation with excitation frequency. Angle of attack: 30°; □ leading edge flap actuation; △ trailing edge flap actuation.

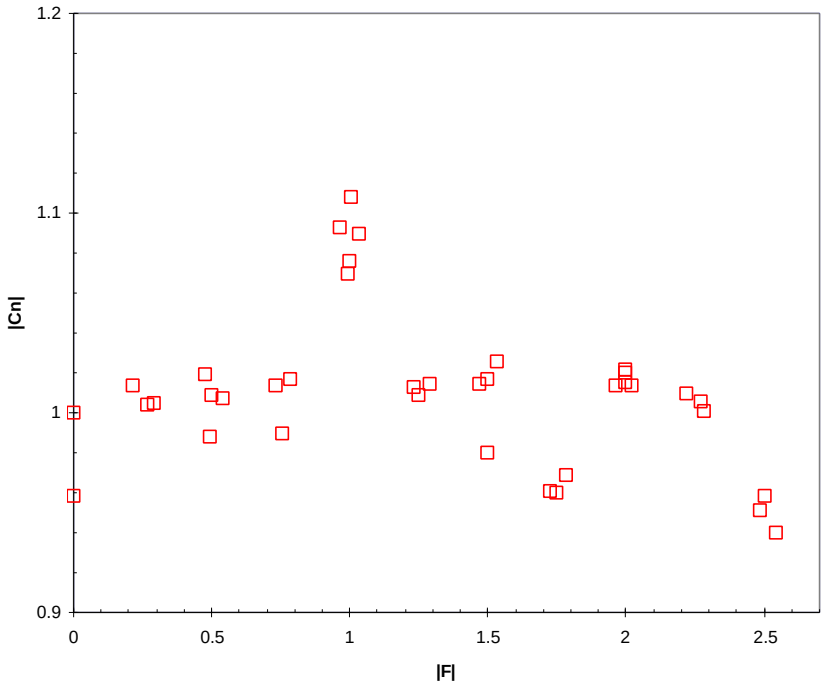

Figure 5.3.2.5 Normal force coefficient variation with excitation frequency. Angle of attack: 25°; leading edge flap actuation.

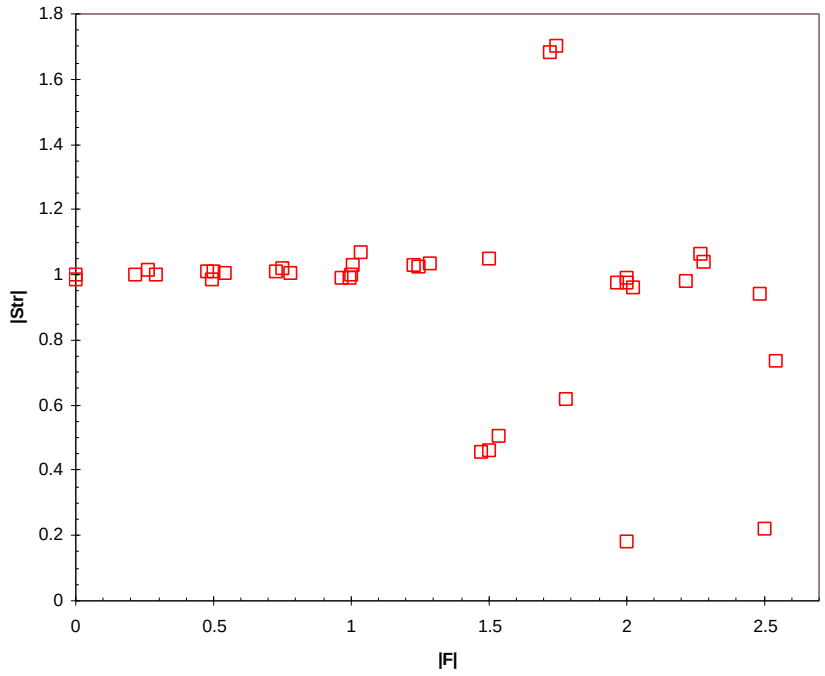

Figure 5.3.2.6 Strouhal number variation with excitation frequency. Angle of attack: 25°; leading edge flap actuation.

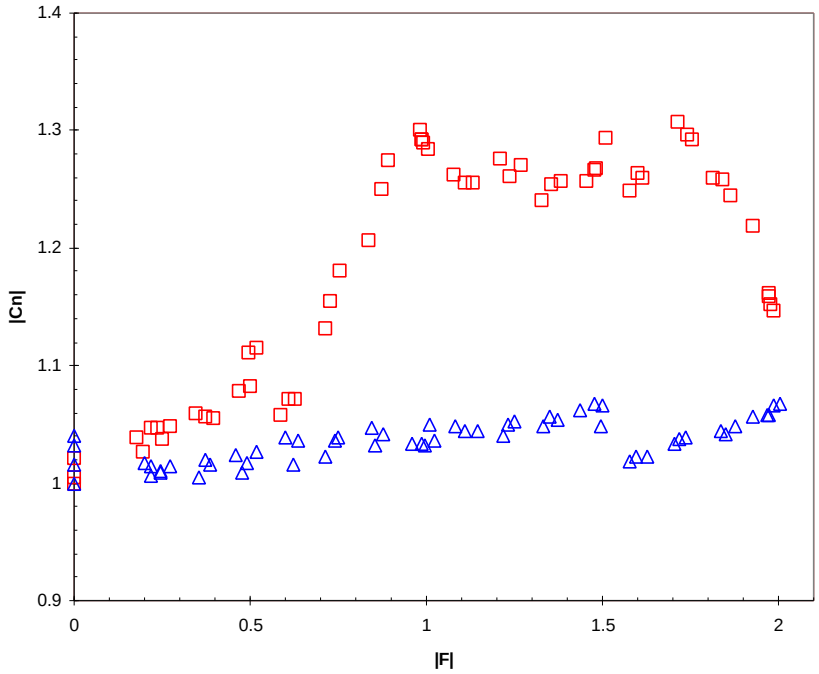

Figure 5.3.2.7 Normal force coefficient variation with excitation frequency. Angle of attack: 20°; □ leading edge flap actuation; △ trailing edge flap actuation.

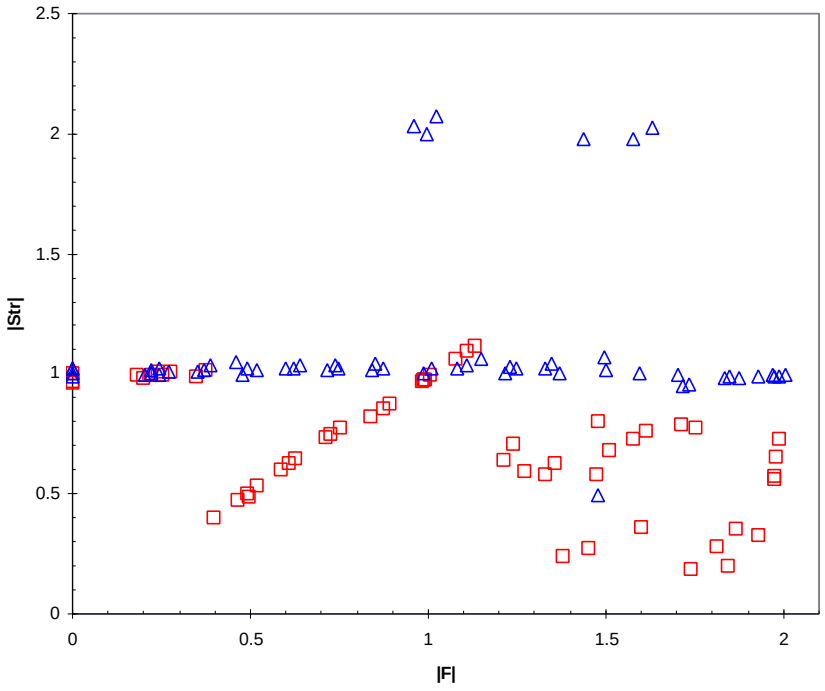

Figure 5.3.2.8 Strouhal number variation with excitation frequency. Angle of attack: 20°; □ leading edge flap actuation; △ trailing edge flap actuation.

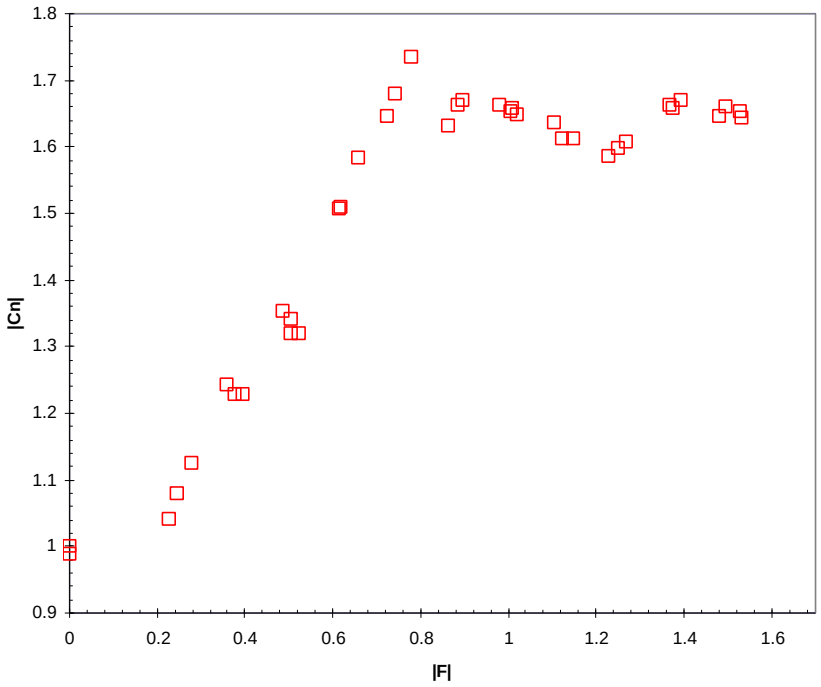

Figure 5.3.2.9 Normal force coefficient variation with excitation frequency. Angle of attack: 15°; leading edge flap actuation.

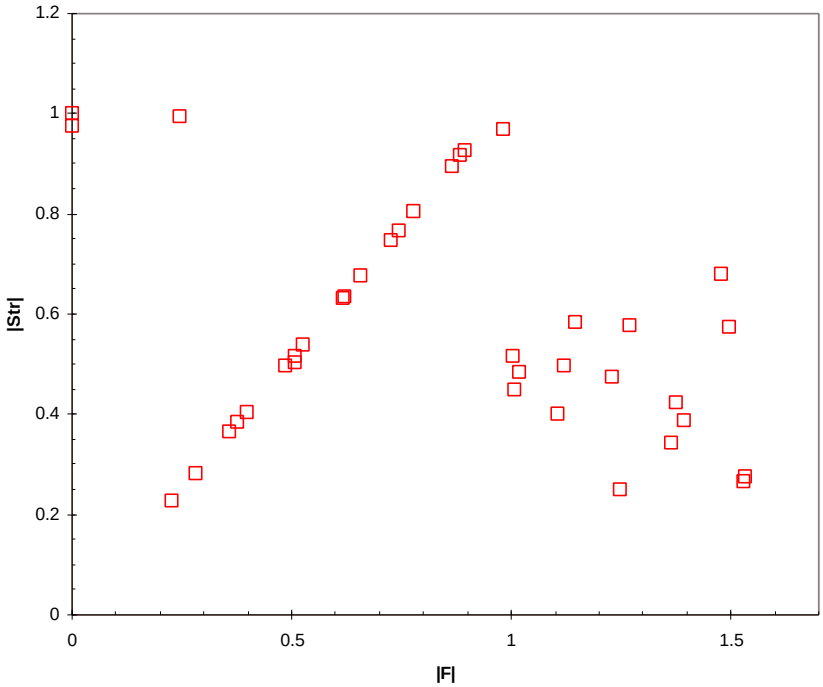

Figure 5.3.2.10 Strouhal number variation with excitation frequency. Angle of attack: 15°; leading edge flap actuation.

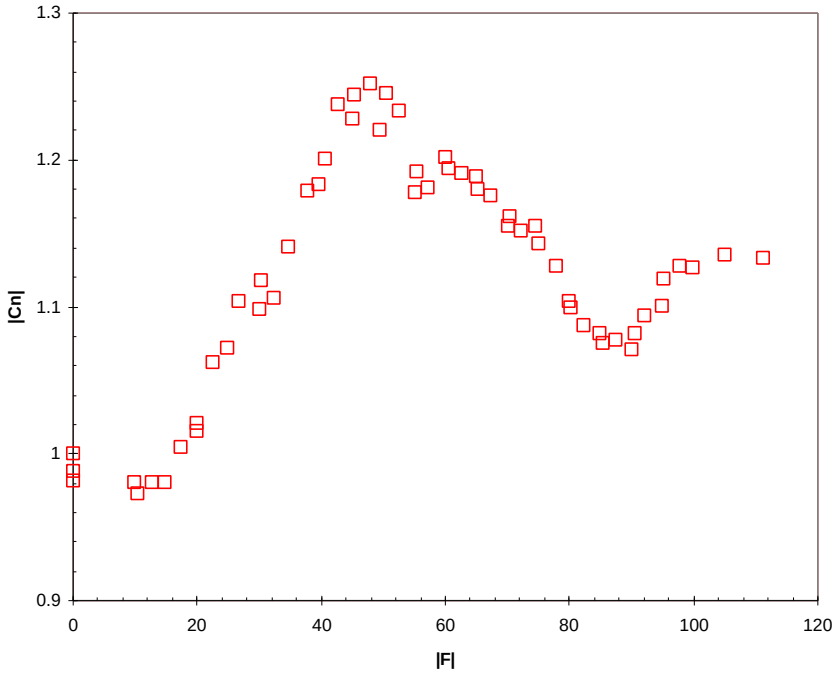

Figure 5.3.2.11 Normal force coefficient variation with excitation frequency. Angle of attack: 10°;leading edge flap actuation.

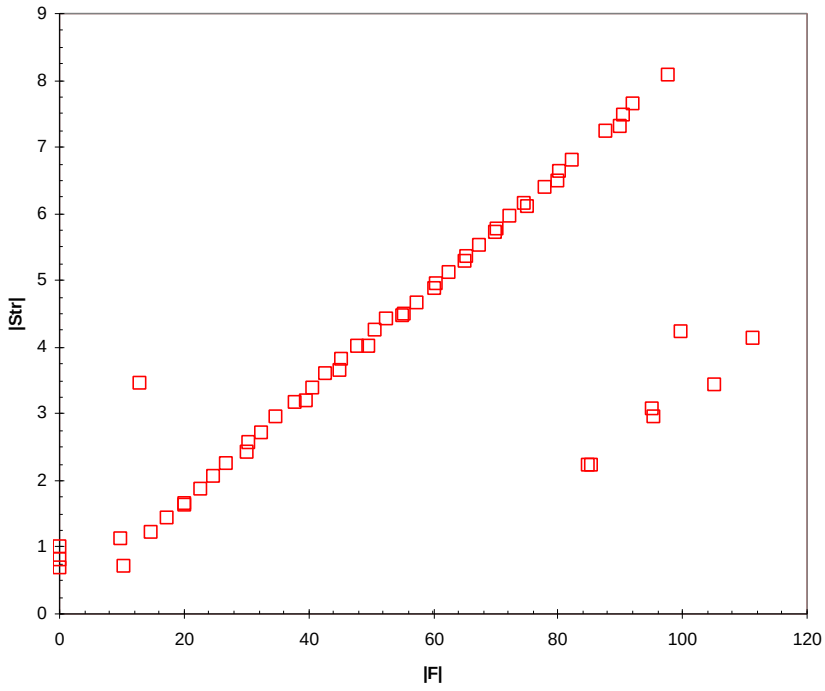

Figure 5.3.2.12 Strouhal number variation with excitation frequency. Angle of attack: 10°; leading edge flap actuation.

Many interesting conclusions can be drawn from the previous figures. The post-processed data can be divided in two categories with respect to the actuation effectiveness. One is the 'higher' angle of attack regime: 25, 30 and 40 degrees; and the other is the 'lower' angle of attack regime: 20, 15 and 10 degrees. Lift increases in the higher angle of attack regime are not as pronounced. Only a 10 percent increase is achieved in the best case for both the 40° and 25° angles, whereas the 30° case doesn't even reach those levels. This is quite disappointing, but is expected from the predictions made by Wu *et al* (1998), where they state that the angle of attack can not be too close to the stall angle, neither too large. At the same time, it is interesting to note that the trailing edge results contradict the predictions of the same authors on the most effective placement of the excitation source, at least for the higher angles regime. The leading edge shear layer control, should be the best actuation due to the upstream location, the highly flexible receptivity and the only source of lift. This is probably true only for the angle of attack range that they refer to. In the current results, the trailing edge flap gives for the 30° case the only source of lift increment.

Both 30° and 40° cases show also a very interesting behavior. As the experiment was repeated to confirm the repeatability of the results, it was observed that a notable dispersion was obtained. This source of dispersion can be attributed to two causes: measuring errors, or particular aerodynamic characteristics of the experiment. At a beginning, the former was suspected. But a closer look at the data might induce some doubt about this conclusion. These cases create the highest pressure values on the surface of the airfoil, thus reducing the accuracy error on the pressure sensor. This and the fact of the different results obtained for the trailing edge actuation, indicates the presence of a particular aerodynamic effect on the airfoil model. A hysteretical behavior could be the cause of this generated pattern.

Transition from the higher to the lower angles of attack seems to be in the proximity of 20° to 25° angle of attack. No effective frequency can be extracted from the 30° or 40° results. A net increase, although small, can be seen for the 25° case on the reduced frequency equal to 1, as predicted by several authors.

Normalized Strouhal numbers analysis shows that no effective frequency changes present. For the angle of attack of 40°, no changes are seen whatsoever. This leads us to conclude that the strong natural vortical structure is not affected by the excitation.

As it can be seen, some normalized Strouhal values in the 30° and 25° angles of attack make the plots more disperse. These automatically calculated points were not 'cleaned' on purpose. Two magnitude close peaks in the PSD calculation for the shedding frequencies are present in these cases, and the selection of the highest magnitude value is subjective. This tells us that the flow is somehow affected by the excitation, with the organized structure reflecting some changes, but not as many as to modify the whole flow field. Figure 5.3.2.4 shows shedding frequency shifting to the first harmonic or the subharmonic of the uncontrolled vortex shedding. Figure 5.3.2.6 is more affected by the excitation frequency, with shifting to the subharmonic values of the natural shedding frequency, some locking-in to the excitation frequency, and the rest at low shedding frequencies relative to the base case.

An example is depicted in Figures 5.3.2.13 and 5.3.2.14 that shows the PSD for two cases, one in the 30° angle of attack, and the other in the 25° angle of attack. For both

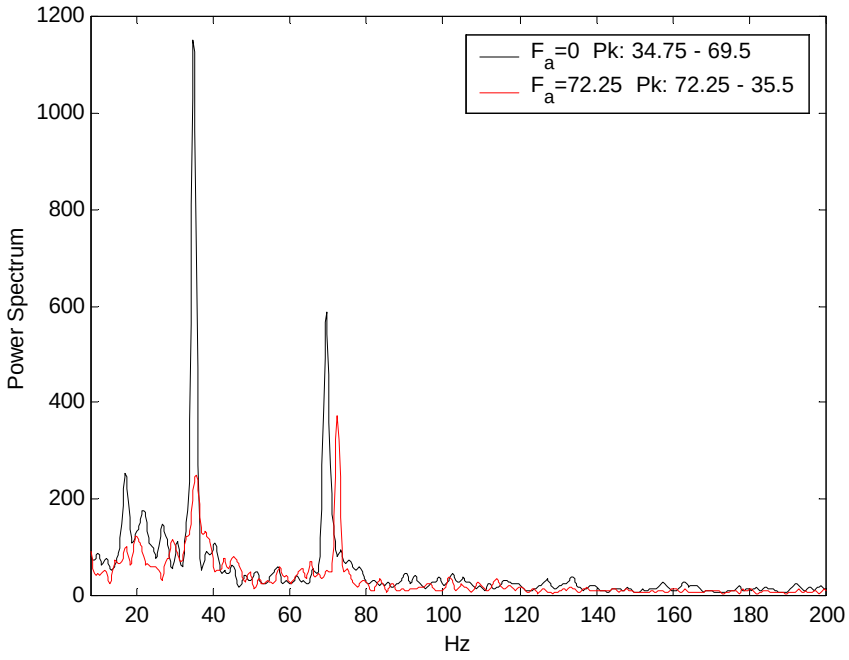

Figure 5.3.2.13 PSD of pitot 3 at excitation |F|=2.06. Angle of attack 30°

cases, a frequency lock-in takes place, but with different effects. From the Figure (5.3.2.13) it can be seen that the excitation frequency organizes the vortical structure locking the vortex shedding to the actuator frequency. Magnitude levels are overall lower,

implying that the vortex structure is weaker than in the base flow. The second figure is even more interesting. A frequency lock-in exist for a non-related natural flow frequency. Not only the shedding locks into this new value, but the vortical formation is completely destroyed into a broader spectrum of vortices. This is the opposite of the desired goal.

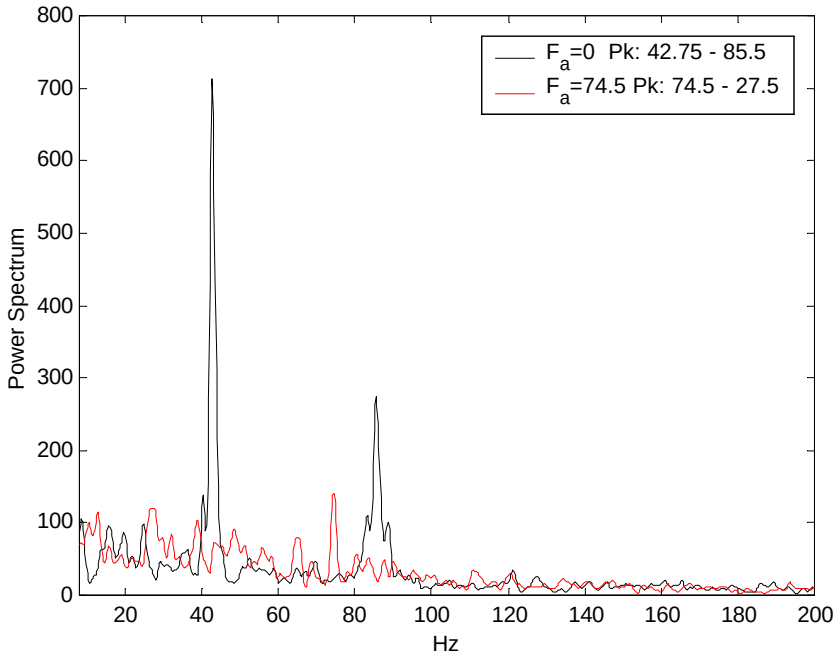

Figure 5.3.2.14 PSD of pitot 3 at excitation |F|=1.75. Angle of attack 25°. Pk: peaks.

Results for the 'lower' angles of attack are completely different to those of the 'higher'. Not only the excitation effect is effective, but also lift increments of up to 73% are achieved. This can be seen in Figure 5.3.2.9 for the15° angle of attack.

The fluid flow excitation at the 20° angle of attack shows a particular behavior in the normal force coefficient for each actuation frequency of the flap. In the range of the reduced frequency from 0 to 1 the normal force coefficient increases almost linearly, with a small peak located at the subharmonic of the natural shedding frequency, and reaching a maximum of 30% increase at the harmonic. Normal force increase is accompanied by a frequency lock-in starting in |F|=0.4 and continuing until |F|=1.13, as shown in Figure 5.3.2.8. The normalized normal force coefficient has a maximum of around 25% increase between the range of 1 through 1.75 of |F| dropping down afterwards. The Strouhal

number after the lock-in region drops down to a value of around 0.5, showing a radical change in the vortex shedding pattern.

Pressure coefficient distribution over the airfoil at this angle of attack is shown in Figure 5.3.2.15, and the corresponding PSD plot in Figure 5.3.2.16. Figure 5.3.2.15 shows that both values of reduced frequency 1 and 1.5 promote the same lift increment, but with a difference in the vortex structure on the suction side of the airfoil. The pressure distribution on the suction side of the latter is slightly higher for the first 50% of the chord and slightly drops down towards the trailing edge. The excitation at the natural shedding frequency behaves at the opposite way, the C_p increases slightly towards the trailing edge. This implies that a different mode of vortex formation is promoted, with the latter being formed towards the trailing edge. This effect has an important implication on the moment coefficient of the airfoil. A change in excitation frequency can shift the position of the aerodynamic center, and at the same time retain the same magnitude.

It is also important to note how the overall change in circulation due to lift augmentation is being reflected in the pressure side, by shifting the pressure coefficient somewhat downwards.

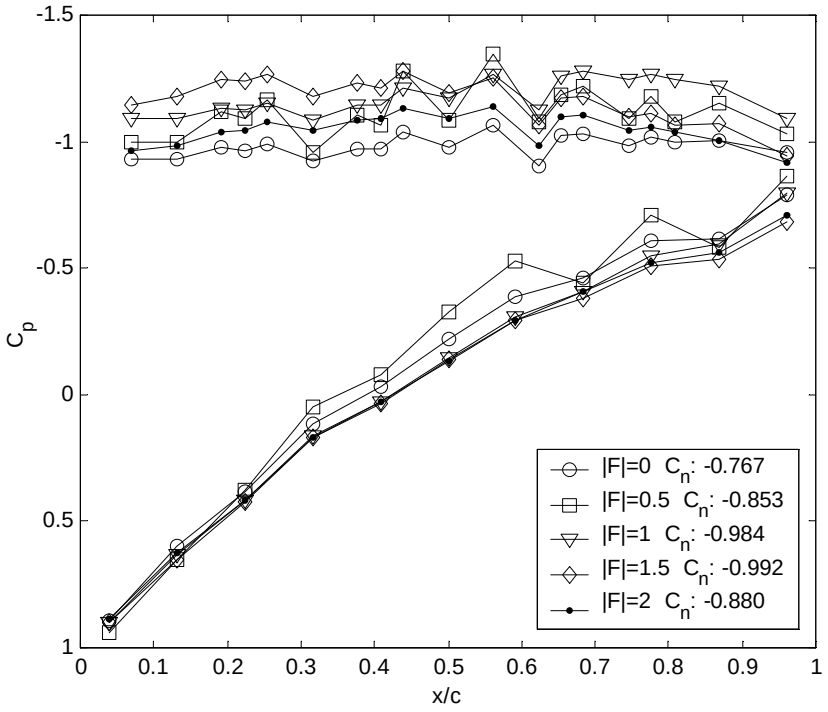

Figure 5.3.2.15 Pressure coefficient distribution for controlled case. Angle of attack 20°. Leading edge excitation.

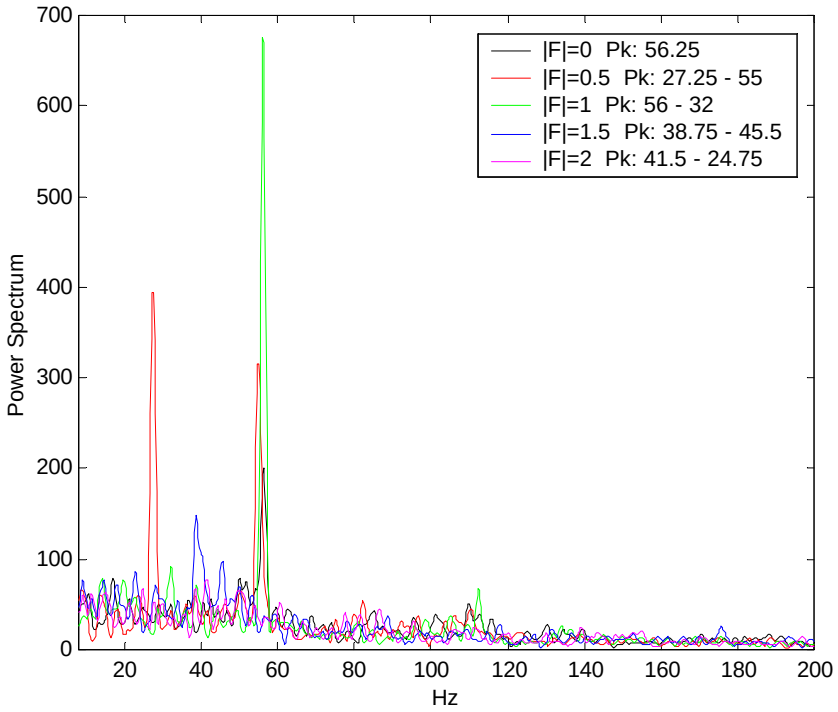

Figure 5.3.2.16 PSD of pitot 3 for controlled case. Angle of attack 20°. Leading edge excitation.

The vortex organization can be seen in Figure 5.3.2.16. There is no doubt that the excitation at the natural frequency of the vortex shedding organizes the flow structure in its resonant mode, and becomes quasi periodic in time. A coherent structure is formed seen on the narrow band peaks on the fundamental frequency and close to subharmonic and first harmonic.

The case for |F|=1.5 corresponds to a completely different level of flow structure. The peaks are not so clear, describing a less organized flow, and with a broader vortex frequency. This might be even beneficial if the pressure oscillation levels are reduced by avoiding bigger vortices to be shed. That would be the ideal: maintain a big vortex in the average over the airfoil suction side, but shedding smaller vortices at a higher frequency. To measure this effect, Figure 5.3.2.17 shows the evolution of the normal force coefficient with time for the different excitation levels. No specific conclusion can be drawn from the figure, but it appears that all excitation frequencies seem to magnify the pressure oscillation levels.

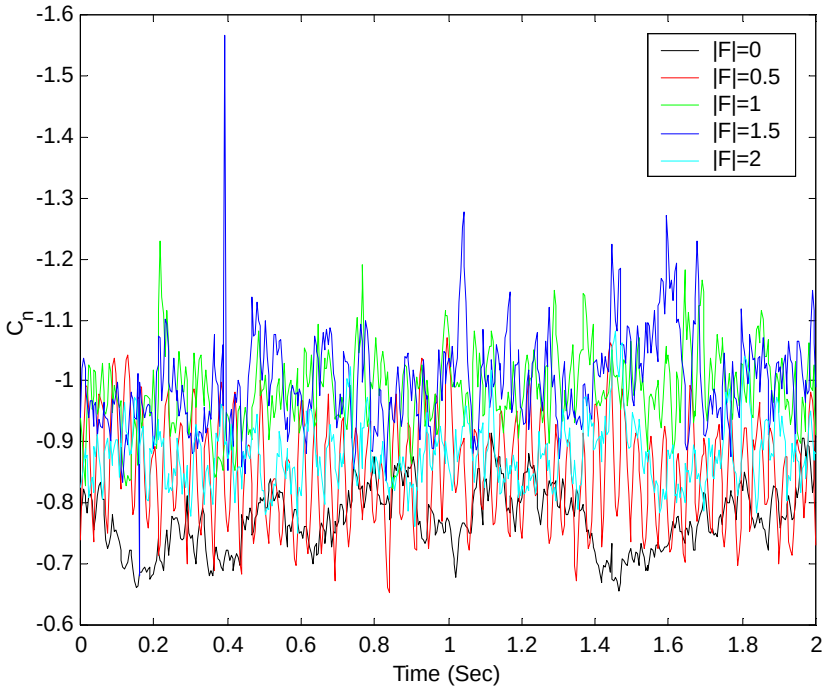

Figure 5.3.2.17 Evolution of normal force coefficient for different actuation frequencies. Angle of attack 20°. Leading edge excitation.

The reduced flap frequency set at the subharmonic shedding frequency affects the airfoil C_p distribution in a distinctive particular mode. Various C_p peaks imply a dense vortical structure in the suction side, and even on the pressure side. As seen on Figure 5.3.2.16 the flow is coherent, with two main frequencies governing the vortex organization. This could be related to two unstable vortices formed on the suction side and alternatively shedding. This 'duality' makes the pressure distribution to oscillate more dramatically, as shown in Figure 5.3.2.17, although being clearly periodic in its behavior.

Trailing edge flap actuation does not affect the flow considerably, with a maximum lift augmentation of 6% at |F|=1.5 and repeated at |F|=2 as seen on Figure 5.3.2.7. Vortex shedding is not modified unless for the reduced frequencies of 1 and 1.5, where the vortices seem likely to shed also at the subharmonic and first harmonic of the natural shedding values. It is interesting to note that the excitation frequency of the trailing edge flap at the reduced frequency of 1.5 affects the flow in such a way that any of the main components (subharmonic, shedding and first harmonic) subsist in the vortical structure over the airfoil. Figures 5.3.2.18, 5.3.2.19 and 5.3.2.20 show the corresponding plots for the trailing edge flap actuation.

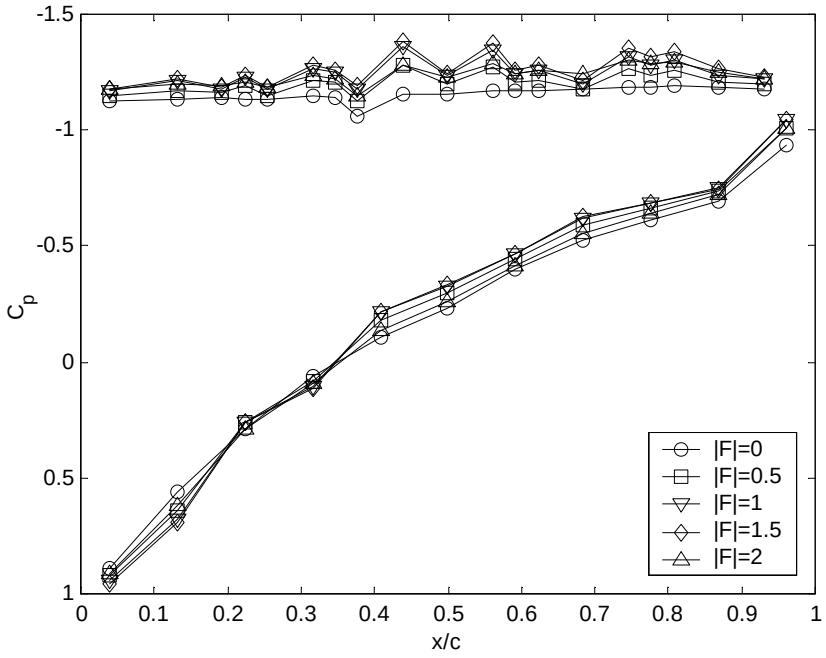

Figure 5.3.2.18 Pressure coefficient distribution for controlled case. Angle of attack 20°. Trailing edge excitation.

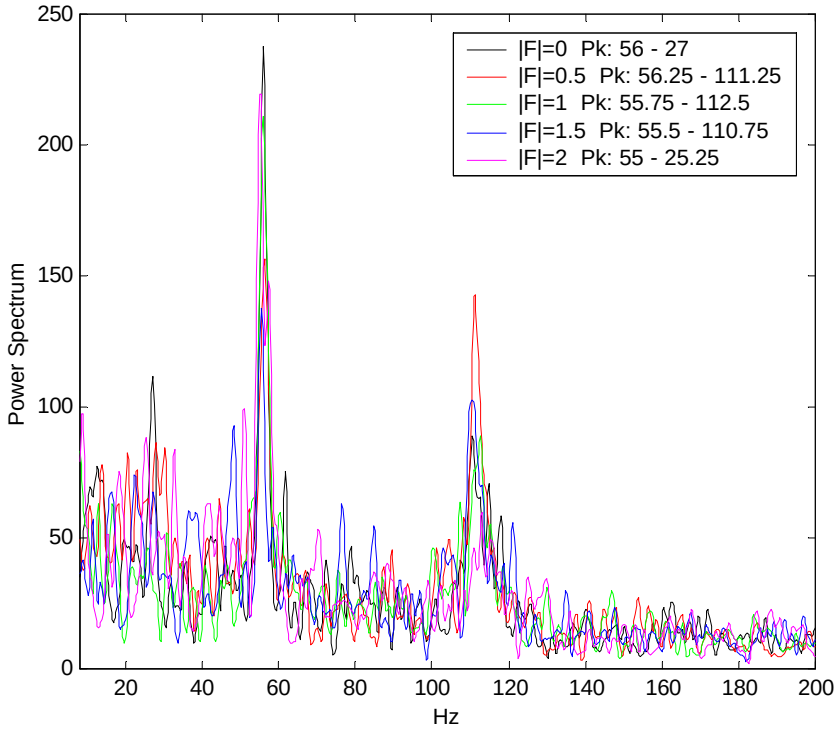

Figure 5.3.2.19 PSD of pitot 4 for controlled case. Angle of attack 20°. Trailing edge excitation.

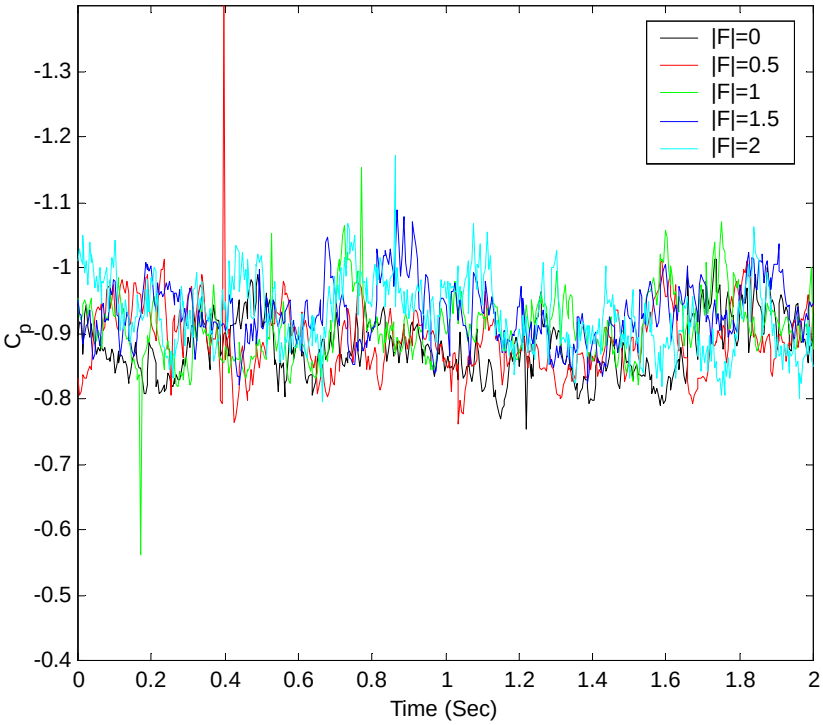

Figure 5.3.2.20 Evolution of normal force coefficient for different actuation frequencies. Angle of attack 20°. Trailing edge excitation.

It can be seen from the figures that the actuation effect is minimal on all aspects. Pressure distribution displays a mild change around 50% and 80% of the chord. Besides that, no other effect is visible. Power spectrum density shows that no real beneficial effect is achieved over the organization of the vortical flow. One of the explanations for the lack of effectiveness is that the global instability originating at the flap triggers a resonant mode with the leading edge shear layer, shifting the rolling up mode at a different frequency, but not really strengthening the vortex structure. The most probable explanation for this behavior is the simple fact that the shear layer is away from the flap, and can not effectively reach it.

The 15° angle of attack generates the maximum lift increase on the airfoil, obtaining a 73% lift increment for a reduced frequency of ~0.75, as shown in Figure 5.3.2.9. The attractive fact is that the lift increases linearly from the lowest reduced flap frequency tested to the most efficient one. This linearity is really useful if control of an aircraft is desired. After its highest value, the normal force coefficient settles in an average value of 1.63, showing some slight variations with flap frequency.

The Strouhal number plot in Figure 5.3.2.10 shows that the linear increase is accompanied with a perfect frequency lock-in to the excitation frequency. This lock-in phenomenon extends up to the frequency of natural vortex shedding. After that, the shedding frequency drops to an average of the subharmonic value. Figures 5.3.2.21 through 5.3.2.23 show the change in the relevant parameters with actuation frequency for the 15° case.

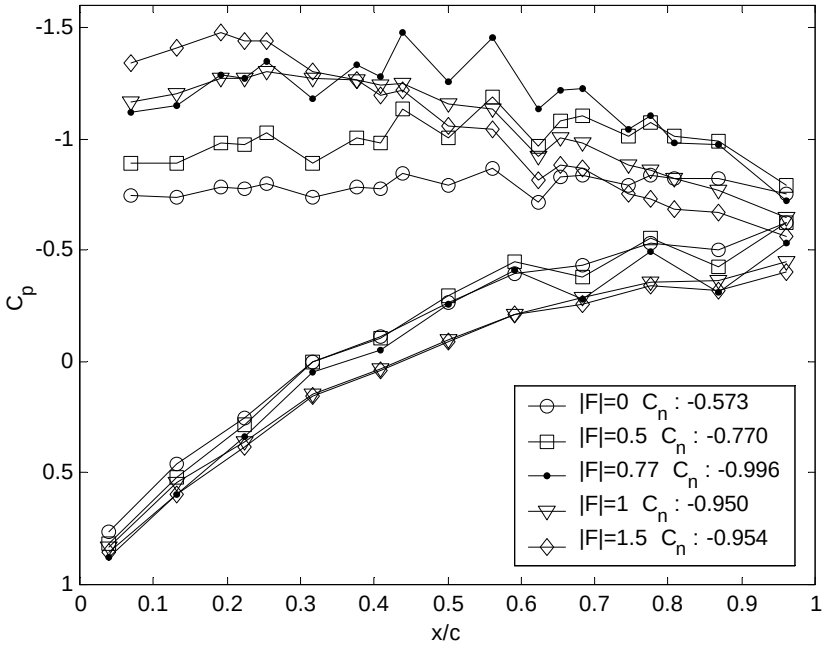

Figure 5.3.2.21 Pressure coefficient distribution for controlled case. Angle of attack 15°. Leading edge excitation.

As it can be seen from the pressure distribution over the airfoil, reduced frequencies 0.5 and 0.77 lead to raising of the suction side pressure distribution, i.e. increasing lift. It is hard to tell, but it would seem that a vortex positioned at half the chord of the airfoil gains strength with the excitation levels. The remarkable point is that an average reattachment close to the trailing edge appears to be present. This fact can be seen by simply extrapolating the measured values for both the suction and pressure side, and checking that the Kutta condition is satisfied.

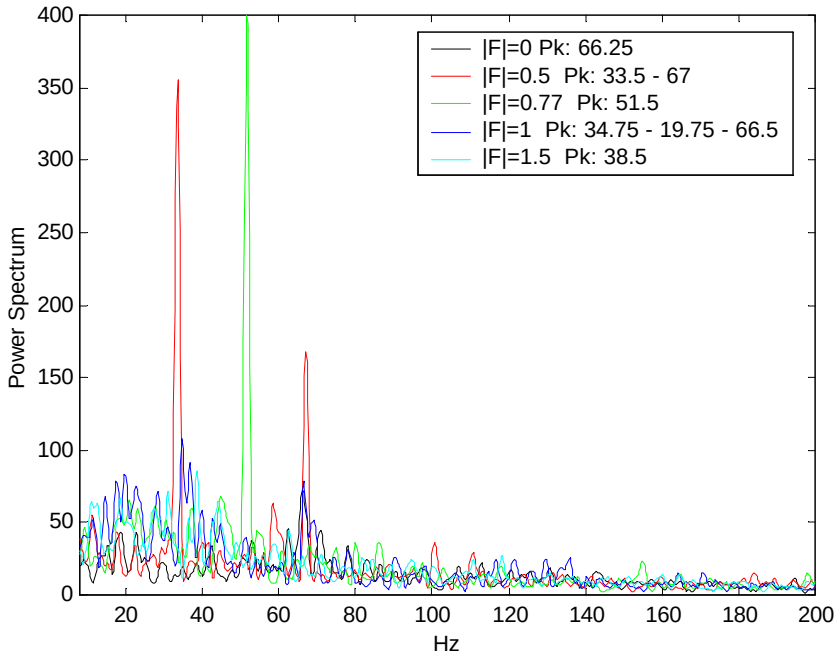

Figure 5.3.2.22 PSD of pitot 3 for controlled case. Angle of attack 15°. Leading edge excitation.

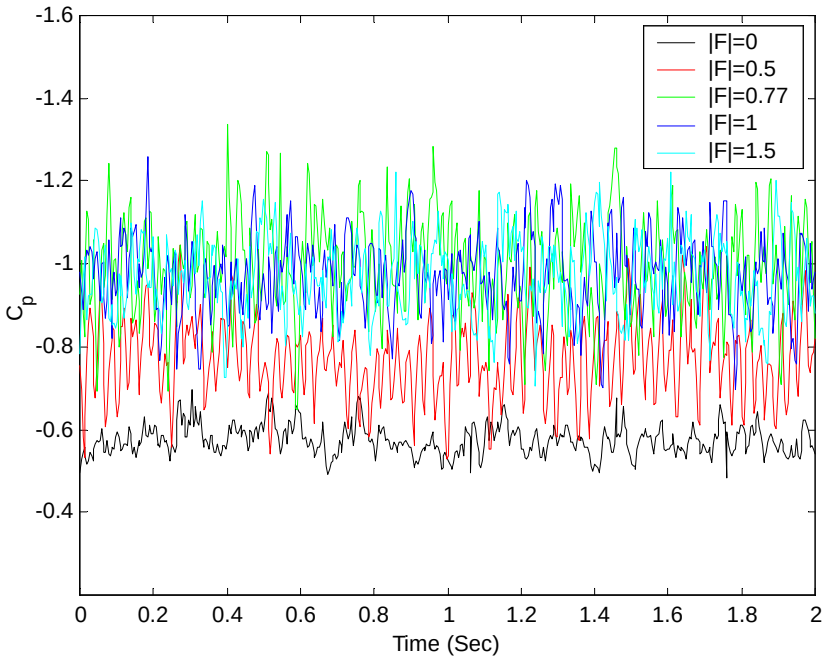

Figure 5.3.2.23 Evolution of normal force coefficient for different actuation frequencies. Angle of attack 15°. Leading edge excitation.

For the higher actuation frequencies, |F|=1 and |F|=1.5 the behavior found in the 20° case is also observed. For |F|=1 there is a tendency for spreading the pressure distribution along the extent of the chord, whereas for |F|=1.5 a suction peak at about 0.2 x/c develops. Both |F|=1 and |F|=1.5 experience as for the 20° case the pressure side pressure increase.

Looking at the PSD plot, it can be seen that for the optimum frequency, a very coherent flow is achieved. A very narrow band frequency implies an organized vortical structure on the suction side of the airfoil, and the magnitude is the reflection of a strong enhanced vortex. It is of interest to note that the frequency at which the vortex is enhanced is not related to the natural shedding frequency.

For the subharmonic excitation, the subharmonic and the natural shedding frequencies are visibly enforced. The higher excitation frequencies don't organize the flow as the ones discussed so far. The frequency spectrum for the latter has broader peaks and of small magnitude.

Figure 5.3.2.23 indicates again the trend seen for previous angles of attack, that when lift increases are obtained, the oscillation amplitude increases too.

The last angle of attack, 10°, shows in Figure 5.3.2.11 a different behavior of the flow control in the circular-arc airfoil. As mentioned before, this case did not show a natural shedding frequency. The calculated one should lie around 100 ~ 110 Hz.

As control is applied, the effect found on the normalized normal force coefficient is similar to that of the 15° case. The difference is that the steady increase of |Cn| with frequency until a maximum of 25%, is followed by a steady decrease up to a value of 7%. Then, a new increment of the normal force occurs and settles at 15%. This strange nonlinear behavior could be explained from the Strouhal number plot. It's clear that a perfect frequency lock-in is enforced on the shedding frequency. That frequency lock-in is extended until a maximum frequency of around 95~97 Hz is reached. The frequency is close to the predicted (extrapolated) shedding frequency. This is not really a coincidence. The changes in the trends of |Cn|, i.e. increasing or decreasing values, occur at the subharmonic or the natural frequency. If we assume that 95~97 Hz is the natural shedding frequency, then the most efficient point occurs at the subharmonic frequency of shedding. Similarly, the second increase of lift settles down to a maximum at around the uncontrolled predicted shedding frequency.

This implies that at 10° incidence the flow requires a perturbation to trigger the shedding of the vortices on the suction side of the airfoil. A stable mode can be converted to an unstable more efficient mode.

Normal force coefficient increments are not as impressive as on the 15° case, but overall lift is augmented. Figures 5.3.2.24 through 5.3.2.26 show the effects of excitation in this particular case.

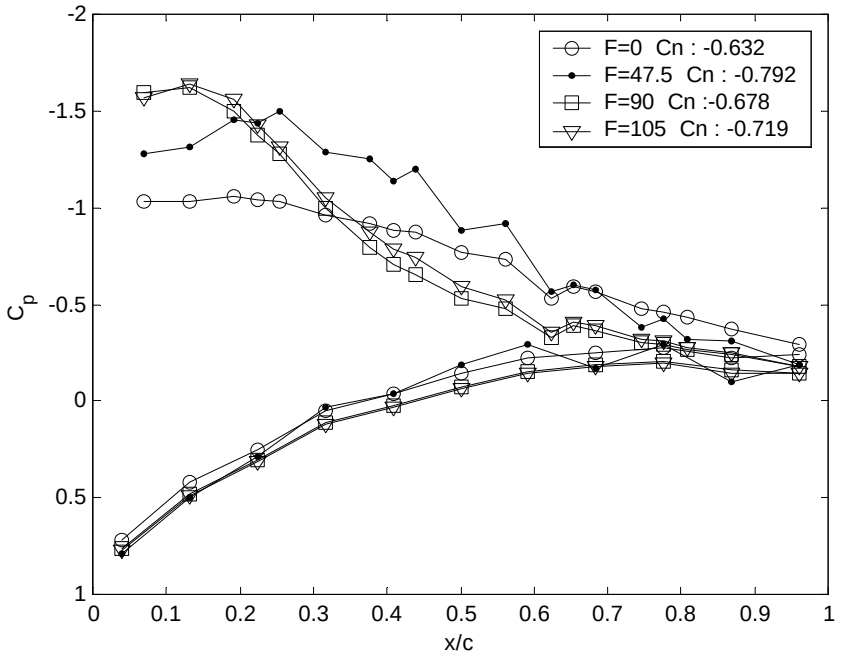

Figure 5.3.2.24 Pressure coefficient distribution for controlled case. Angle of attack 10°. Leading edge excitation.

From the results, it can be seen that the only frequency that really triggers the shedding phenomenon is that of the predicted subharmonic flap frequency. This appears clearly from the PSD plot in Figure 5.3.2.25. From there, the frequency lock-in is visible, but also a component at twice that frequency, namely the estimated natural vortex shedding. For the other excitation values, the flow structure is not enhanced, as can be seen from the broad frequency spectrum.

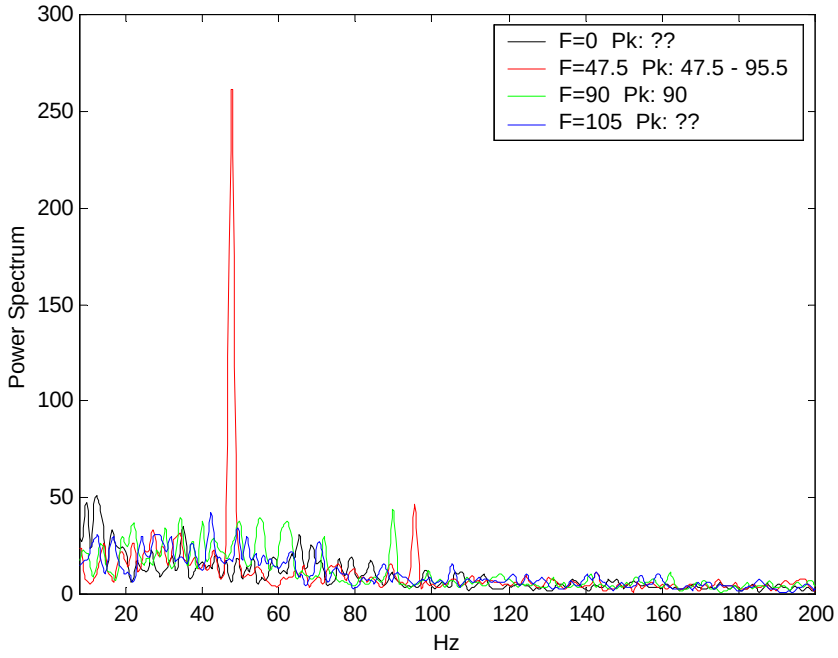

Figure 5.3.2.25 PSD of pitot 3 for controlled case. Angle of attack 10°. Leading edge excitation.

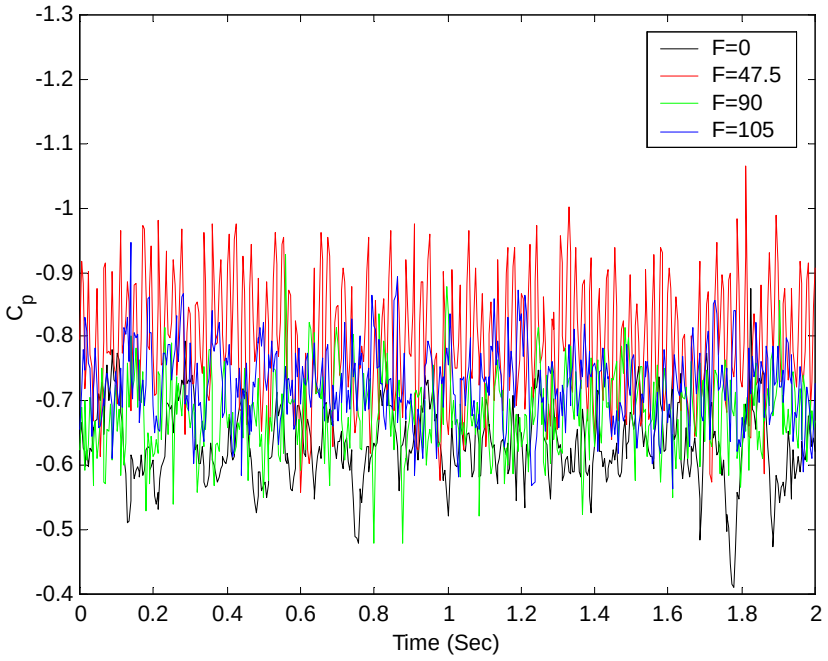

Figure 5.3.2.26 Evolution of normal force coefficient for different actuation frequencies. Angle of attack 10°. Leading edge excitation.

Pressure distributions are also unexpected and unusual. While the highest reduced frequencies seem to promote a fast reattachment of the flow, the optimum reduced frequency creates a vortex in the average sense over the suction surface, that increases the suction force. This can be seen in Figure 5.3.2.24. Flow is reattached also in the average sense, but at a further downstream point. The plot of the airfoil pressure coefficient with respect to time, shows again that excitation increases oscillation amplitude.

It's interesting to remark that the classical thinking of the improvement of separated flow by forcing reattachment, does not necessarily mean that it will generate the largest lift (case |F|=47.5). If periodic excitation is applied, it is possible to capture a large vortex in the average and therefore provide even more lift than the fully attached flow case.

5.4 Balance Results

Balance force measurements were not as successful as expected. Many problems were found related to the unsteadiness of the flow. In order to obtain good results by utilizing a balance system, a fairly rigid system is needed to eliminate the possibility of oscillations of the tunnel model induced by the separated flow. This of course has a limiting factor imposed by the resolution of the sensor measuring the applied forces. If a very stiff balance system is used, then signals coming from the strain gages are very weak, and either high signal amplification or a high-resolution acquisition board is needed. Amplifying the signals by a large factor is always avoided since noise is introduced, and a high-resolution board, besides being expensive, carries also a performance limit. Therefore, a compromise exists between the experiment to be conducted and the tools available to perform it. In the current research, this compromise could not be satisfied.

Experiments for the balance were conducted at different speeds and with and without pressure acquisition. These were acquired to quantify the effect of the balance oscillation on the flow field.

As previously mentioned before the balance was not calibrated, and since relative results with respect to the base case are required, it does not affect the experiment. All data acquired is shown in the form of an amplified voltage signal, proportional to the forces excerpted on the balance system. It would be difficult to understand all the highly nonlinear signals coming from the available six channels at the same time, but two of them, clearly show the lift and drag forces acting on the airfoil model. We take these signals as the present point of comparison.

First of all, it is important to take a look at the natural frequencies of the complete airfoil model. This can be easily performed introducing a perturbation in the model and letting it oscillate freely. The frequency spectrum is the same for both lift and drag channels, and shown in Figure 5.4.1.

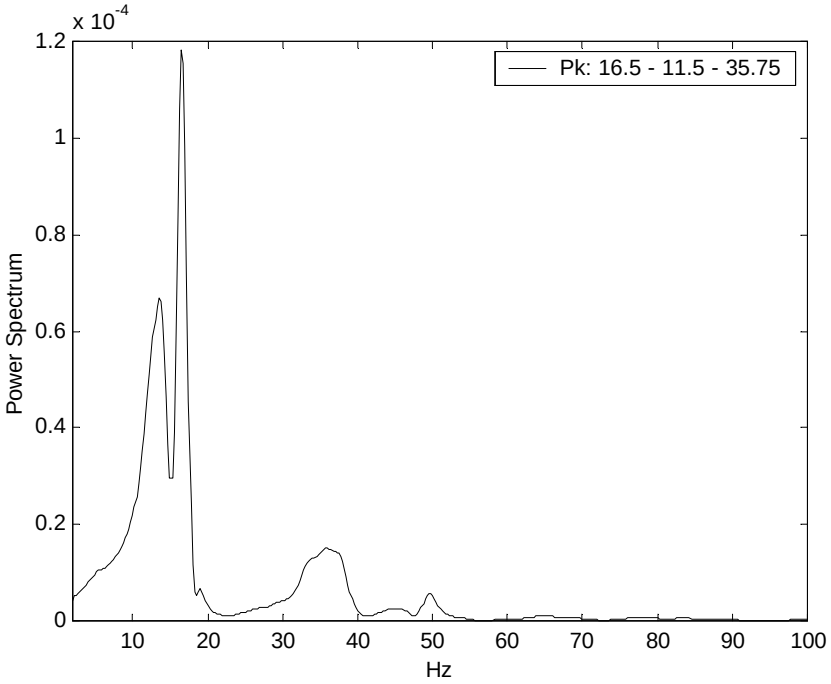

Figure 5.4.1 Natural frequency spectrum for the balance system.

The figure shows that the resonant frequency is at 16.5 Hz. Test performed at 10 m/s and at an angle of attack of 40° indicated that the oscillations induced by the separated flow over the airfoil model were considerable. This is obvious due to the fact that the shedding frequency was 17.5 Hz. There is a serious doubt on the accuracy of the natural shedding frequency. Using the Strouhal number for the clamped balance case, the resulting frequency should be 16 Hz. There is an evident aeroelastic coupling present.

The solution is to perform the experiment away from the resonant frequency by increasing speed or decreasing angle of attack. A test at 30° and 10 m/s showed a better agreement of the Strouhal number with the clamped case. A proof was performed comparing the evolution of the integrated pressure distribution over the suction side of the airfoil. All suction side taps were utilized for this purpose, and the result are shown in Figure 5.4.2. It can be seen that there is a good correlation between both cases, maintaining the same average value. Even when this seemed promising, the results from the balance were not perfect. This can conclusion can be extracted by looking at Figure 5.4.3. There exist

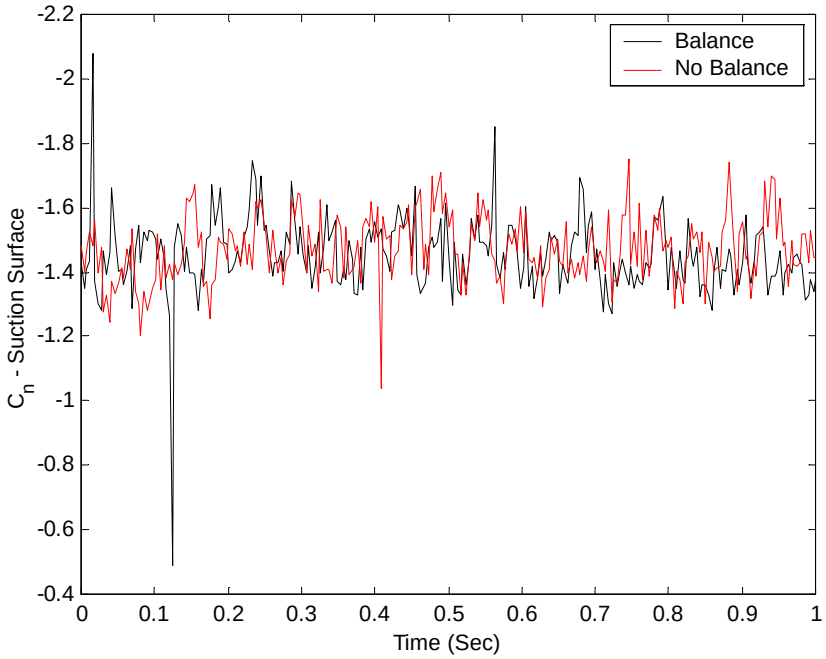

Figure 5.4.2 Integrated pressure over the suction side of the airfoil. $a = 30°$, $U_\infty = 10\ m/s$.

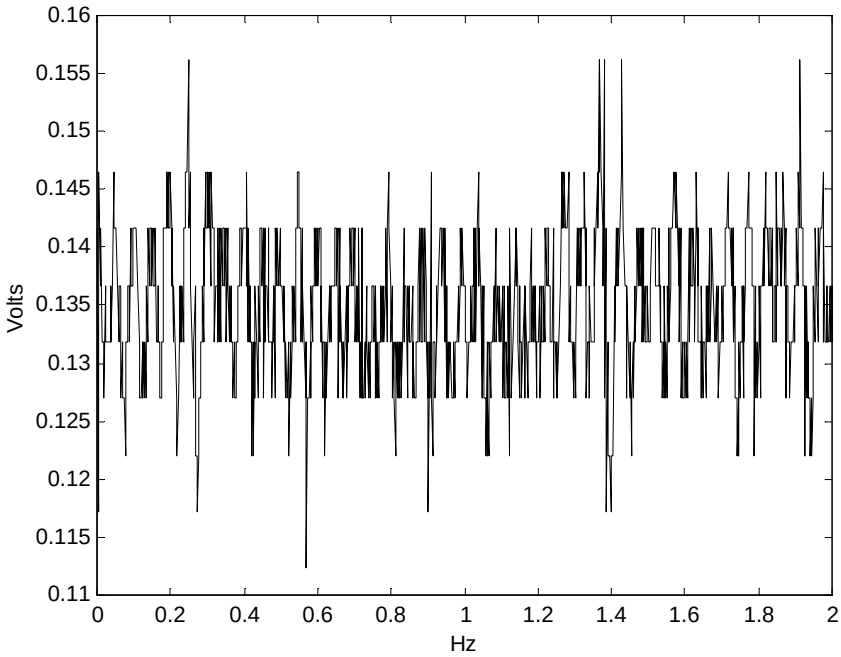

Figure 5.4.3 Balance output voltage for the lift channel. $a = 30°$, $U_\infty = 10\ m/s$.

resolution problems in the signal originated in the board. For the RCE board, having a 12-bit resolution over a non-adjustable range of ±10 Volts, is of 0.004882 Volts, exactly the resolution deficiency seen.

The solution for this problem, besides replacing the board (which was not possible), is to increase the tunnel free stream speed. This was performed, but again, the oscillation levels increased, now due to the increment in magnitude of the forces applied on the model and its intrinsic rigidity. The measured pressures were drifting excessively from the clamped balance case, as also seen on the 40° test, and no solution was found.

The clear alternative is buying a high resolution, adjustable range acquisition board, to fit the balance in the experiment.

A question could arise on why a heavier model wasn't tested, or damping wasn't provided to the balance. The answer to this question is simple. It was part of the research to see the evolution of the forces/pressures with respect to time. A heavy model or damping, would had averaged the forces, and give a fairly constant signal with respect to time. This would lead to small amplitude measurements limited again by the board resolution.

It can be seen that the design and implementation of a balance for unsteady measurements is complex, and experiment dependent. More research needs to be performed in order to give a final, user-friendly and forgiving measuring tool.

Chapter 6 Conclusions and Proposed Work

It was shown that lift augmentation in the post-stall range of supersonic airfoils in subsonic regimes is possible. Lift augmentation of up to 70% for the 15° angle of attack was achieved. The rolling up vortex process over the airfoils suction side was effectively controlled by means of a periodically oscillated flap on the leading edge. This excitation provided a form of organizing the vortical structure present in the separated region. The coherent vortices formed promoted the change from a massively separated flow to a closed separation bubble in the average sense, holding a strong vortex on the upper surface on the airfoil that improved circulation. The parametric study showed that this effect was effective in the angle of attack range between 10° through 20° and excitation frequencies close to the natural shedding frequency of the uncontrolled airfoil.

It is still not clear how the flap excitation physically disturbs the flow and why it was not effective at the higher angles of attack. One possibility is that the small perturbation of the shear layer by the flap, did not reach the vortex layer. Wu *et al* (1998) predicted that for the control mechanism to be effective, the vortex should not be far from the surface. Our experiment therefore seems to confirm this. A more careful analysis should be made in order to understand the physics of this behavior. A good non-intrusive measuring method should be utilized to closely see the effect of the flap on the shear layer, and its evolution at different angles of attack.

Another way to eliminate the possibility of the flap not reaching the shear layer is the use of periodic blowing/suction, or synthetic jets. As reported in on the literature, jets can penetrate the shear layer from relatively long distances. Moreover sound streaming would also add to vortex streaming as part of the vortical flow enforcing. In should be mentioned that in this experiment, relatively high sound levels were originated in the flap at the higher frequency range, probably by the collision of the flap and the airfoil in the closed position. However, no quantitative measurements were performed.

The idea of the flap working as a synthetic jet was not analyzed in detail, but it is reasonable to think that the flap could behave as one. This reinforces the fact that a form of perturbing the flow without limitations in reach is needed. The flap is not a practical option due to the frequency limitations present.

A point that definitively needs further research is the effectiveness of introducing the perturbation at the trailing edge. In all of the research done to date the excitation is

introduced at the leading edge. Our results indicate that this is indeed the most effective, but no test was performed on the effect of the perturbation of both vortex layers. As we know, the vortex shedding is formed by a nonlinear local and global interaction. Effects were seen on the trailing edge flap, but were minimal. The effect of simultaneous perturbations is completely unknown.

Periodic excitation is an effective tool, as demonstrated in this experiment and many previous ones. The question is, why not modulate in time the excitation in frequency or in amplitude? A highly non-linear behavior is in process in the suction side of the airfoil. Why should a plain periodic perturbation be the most effective one? Hsiao *et al* (1998) already showed that a different wave form rather than a sinusoidal disturbance improved the vortex structure and therefore lift.

An important factor that still needs to be studied is the Reynolds number effect. Reynolds number should not affect bluff body flows, but still, at the lower angles of attack there exist some uncertainty about the results. Mach number is also an important parameter in flow control to be taken into account. This implies more expensive tunnel testing.

Sweep angles are another important subject that needs to be studied. From the literature, it is not difficult to see that sweep effect is beneficial for the stability of the leading edge vortex, so even better increments should be expected. More important is the effect of finite configurations. In an actual airplane wing, the flow is not two dimensional, and the control could become more cumbersome.

Research still needs to be carried out, and an open door to unexplored areas waits for better ideas and numerous potential applications.

References

Barlow, J. B., Rae, W. H., Pope, A., 1999, “Low-Speed Wind Tunnel Testing”, 3rd edition, Wiley-Interscience publication, John Wiley & Sons, New York.

Bursnall, W. J., 1952, “Experimental Investigation of the Effects of Vortex Generators on the Maximum Lift of a 6-Percent-Thick Symmetrical Circular-Arc Airfoil Section”, NACA RM L52G24.

Chang, R. C., Hsiao, F. –B., Shyu, R. –N., 1992, ”Forcing Level Effects of Internal Acoustic Excitation on the Improvement of Airfoil Performance”, *J. of Aircraft* , Vol. 29, No. 5, pp. 823-829.

Crook, A., Sadri, A. M., Wood, N. J., 1999, “The development and Implementation of Synthetic Jets for the Control of Separated Flow”, AIAA 99-3176.

Fiedler, H. E., 1998, “Control of Free Turbulent Shear Flows”. In *Flow Control: Fundamentals and Practices* (ed. Gad-el-Hak, M., Pollard, A., Bonnet, J. P.), pp. 335-429, Springer Lecture Notes in Physics, New Series Monographs, M53, Springer-Verlag, Berlin.

Gad-el-Hak, M., 1998, “Introduction to Flow Control”. In *Flow Control: Fundamentals and Practices* (ed. Gad-el-Hak, M., Pollard, A., Bonnet, J. P.), pp. 1-107, Springer Lecture Notes in Physics, New Series Monographs, M53, Springer-Verlag, Berlin.

He, Y., Kral, L., 2000, ”Post-Stall Control on an Airfoil Using Localized Jet Actuators”, AIAA 2000-0408.

Hsiao, F. –B., Liu, C. -F., Shyu, J. –Y., 1990,”Control of Wall-Separated Flow by Internal Acoustic Excitation”, *AIAA Journal* , Vol. 28, No. 8, pp.1440-1446.

Hsiao, F. –B., Shyu, R. –N., Chang, R. C., 1994, ”High Angle-of-Attack Airfoil Performance Improvement by Internal Acoustic Excitation”, *AIAA Journal* , Vol. 32, No. 3, pp. 655-657.

Hsiao, F. –B., Wang, T.-Z., Zohar, Y., 1993, “Flow separation Control of a 2-D Airfoil by a Leading-Edge Oscillating Flap”, Intl. Conf. Aerospace Sci. Tech., Dec. 6-9, 1993, Tainan, Taiwan.

Hsiao, F. -B., Liang, P. F., Huang, C. Y., 1998, “High-Incidence Airfoil Aerodynamics Improvement by Leading-Edge Oscillating Flap ”, *J. of Aircraft*, Vol. 35, No. 3, pp. 508-510.

Ho, C.-M., Huerre, P., 1984, “Perturbed Free Shear Layers”, *Ann. Rev. Fluid Mech.,* Vol. 16, pp. 365-424.

Ho, C.-M., 1981, “Local and global dynamics of free shear layers”, In *Numerical and Physical Aspects of Aerodynamic Flows* (ed. T. Cebeci), pp. 521, Springer-Verlag.

Kiya, M., Mochizuki, O., Suzuki, N., 1999, “Separation Control by Vortex Proyectiles”, AIAA 99-3400.

Roshko, A., 1954, “On the Drag and Shedding Frequency of Two-Dimensional Bluff Bodies”, NACA TN 3169.

Schaeffler, N. W., 1998, “All the Kings Horses: The Delta Wing Leading-Edge Vortex System Undergoing Vortex Breakdown: A Contribution to Its Characterization and Control Under Dynamic Conditions,” Ph.D. Dissertation, Virginia Polytechnic Institute and State University, Department of Engineering Science and Mechanics, Blacksburg, Virginia.

Seider, G., 1984, “The Design, Construction, and Calibration of a Low Speed Wind Tunnel”, Report filed for Dr. D. P. Telionis on behalf of the VPI-ESM Fluids Mechanics Laboratory.

Vlachos, P. P., Telionis, D. P., Donnelly, M. J., 1999, “The Design and Testing of a Smart Balance System”, AIAA 99-3165

Wicks, B. H., 1954, “Study of the Subsonic Forces and Moments on an Inclined Plate of Infinite Span”, NACA TN 3221.

Wu, J. Z., Lu, X. Y., Denny, A. G., Fan, M., Wu, J. M., 1998, “Post-stall flow control on an airfoil by local unsteady forcing”, *Journal of Fluid Mechanics* 371, pp. 21-58.

Wu, J. Z., Vakili, A. D., Wu, J. M., 1991, “Review of the Physics of Enhancing Vortex Lift by Unsteady Excitation”, *Prog. Aerospace Sci.,* Vol. 28, pp. 73-131.

Zhou, M. D., Fernholz, H. H., Ma, H. Y., Wu, J. Z., Wu, J. M., 1993, “Vortex Capture by a Two-Dimensional Airfoil with a Small Oscillating Leading-Edge Flap”, AIAA 93-3266.

Vita

Sergio Miranda was born the 8 of January of 1974 to Edgardo Norberto Miranda and Elena Maria Pacholek. Growing up surrounded by model airplanes built by his father, he started to get the taste to flying machines. At age 13, he found in a library a book in aerodynamics, and not even understanding its contents, he knew that was his future.

After graduating from high school, in 1992 he enrolled in the Universidad Catolica de Cordoba. In 1995, he continued his studies in Aeronautical and Mechanical Engineering in the Instituto Universitario Aeronautico. In 1997 he finished his studies getting his diploma from the Universidad Catolica de Cordoba and the Instituto Universitario Aeronautico, obtaining the best GPA in his class and the Instituto Universitario Aeronautico Award.

In 1998 he enrolled the Virgina Polythechnic Institute and State University.

In 1999 he was awarded with the National Academy of Engineers Award (Argentina) to the best Engineering Graduates, for his achievements as a student.

In addition to his interest in Engineering, his other passions include swimming, running, dirt biking, and everything that could challenge him.